Eur. Phys. J. B (2012) 85: 148
DOI: 10.1140/epjb/e2012-20902-0

THE EUROPEAN PHYSICAL JOURNAL B

Regular Article

The Boson peak of model glass systems and its relation to atomic structure

P.M. Derlet[1,a], R. Maaß[2], and J.F. Löffler[2]

[1] Condensed Matter Theory Group, Paul Scherrer Institut, 5232 Villigen PSI, Switzerland
[2] Laboratory of Metal Physics and Technology, Department of Materials, ETH Zurich, 8093 Zurich, Switzerland

Received 4 November 2011 / Received in final form 23 January 2012
Published online 15 May 2012 –

Abstract. Bulk metallic glasses (BMGs) exhibit a rich variety of vibrational properties resulting from significant atomic scale disorder. The Boson peak, which reflects an enhancement of states in the low frequency regime of the vibrational density of states (VDOS), is one such experimental signature of amorphous materials that has gained much interest in recent times. However, the precise nature of these low frequency modes and how they are influenced by local atomic structure remains unclear. Past simulation work has demonstrated that such modes consist of a mixture of propagating and localized components, and have been referred to as quasi-localized modes. Using standard harmonic analysis, the present work investigates the structural origin of such modes by diagonalising the Hessian of atomistic BMG structures derived from molecular dynamics simulations using a binary Lennard Jones pair potential. It is found that the quasi-localized vibrational modes responsible for the low frequency enhancement of the VDOS exist in a structural environment characterized primarily by low elastic shear moduli, but also increased free volume, a hydrostatic pressure that is tensile, and low bulk moduli. These findings are found to arise from the long-range attractive nature of the pair-wise interaction potential, which manifests itself in the corresponding Hessian as long-range off-diagonal disorder characterized by a distribution of negative effective spring constants.

1 Introduction

Amorphous solids, such as network and bulk metallic glasses, exhibit novel thermal properties that have been the focus of significant research activity and vibrant debate [1–8]. Much of the work has been focused on the observation and understanding of the so-called Boson-peak, which historically has been measured via Raman spectroscopy. Indeed when the Raman signal is divided by appropriate temperature and frequency factors the result was found to be temperature independent and proportional to the vibrational density of states (VDOS) divided by the square of the vibrational frequency [9]. Since the proportionality factor between the modified Raman intensity and the VDOS is believed to be a monotonically increasing function of the vibrational frequency, much of the contemporary work has assumed that the Boson-peak seen by Raman is explicitly due to an anomaly in the VDOS, reflecting an enhancement of low frequency states relative to an elastic continuum Debye level. The low frequency at which the maximum occurs is referred to as $\Omega_{\rm BP}$ – the Boson-peak frequency. Importantly, when the Boson-peak is appropriately rescaled with respect to $\Omega_{\rm BP}$ and the corresponding VDOS at $\Omega_{\rm BP}$, its form is found to be largely independent of the material type, suggesting that its underlying origin may be quite fundamental to the physics of scattering in disordered systems.

Contemporary experimental techniques for the measurement of the Boson-peak and the underlying acoustic modes are performed via inelastic neutron or X-ray scattering, both of which can directly probe the dynamical structure factor as a function of both scattering vector and energy transfer. Much of this experimental work involves the investigation of how the dispersion of the experimentally accessible longitudinal acoustic mode deviates from linear behaviour, and how the width of the corresponding dynamical structure factor broadens with increasing frequency/wavevector. Experimentally the line-width of the longitudinal mode, Γ, is found to increase rapidly with vibrational frequency, approaching the so-called Ioffe-Regel limit $\Gamma_{\rm IR} = \Omega_{\rm IR}/\pi$ at frequency $\Omega_{\rm IR}$; a regime where the mean-free-path of a propagating mode is comparable to its wavelength. It has been argued (for and against) that experiment demonstrates a strong similarity between $\Omega_{\rm IR}$ and $\Omega_{\rm BP}$, that is, it is at the Boson-peak region where the acoustic branches terminate [1–8]. One aspect somewhat clouding the emerging experimental picture is that both neutron and X-ray inelastic scattering probe the longitudinal acoustic mode which strongly hybridizes with the acoustic transverse mode for good glass formers, and only

[a] e-mail: peter.derlet@psi.ch

weakly for fragile glasses due to minor (or non-existent) directional bonding. This is an important aspect when considering the results of such experiments, since via Raman scattering those excess vibrational states associated with the Boson-peak appear to be transverse in nature [10,11].

Atomistic simulation has played an important role in the progress to understand the low frequency vibrational properties of amorphous systems. By diagonalising the force matrix of a computer generated amorphous atomic structure, early work using a Stillinger-Weber potential to model a network glass [12] found that there exist low frequency modes which involve a significantly reduced number of atoms in regions of low coordination. In later work using repulsive pair-wise potentials to model soft sphere glasses [13,14] low frequency modes were also found, although a clear connection to local atomic structure, as in the case for network glasses, could not be established. In reference [14] their location did correspond to regions of nearest neighbour compression, but with a somewhat reduced local density. In all these works, it was found that these low frequency-modes depended on system size in that the typical number of atoms involved scaled with volume (the total number of atoms). This conclusion was also reached in the work of Mazzacurati et al. [15], who performed a normal-mode analysis of a Lennard-Jones model glass system as a function of simulation cell size.

The above resuls indicate that the low frequency modes could not be considered truly localized, but rather of a mixed nature involving both propagating modes and localized modes, which are themselves not eigenstates of the system – forming so-called quasi-localized modes. In subsequent work on soft sphere glasses, Schober and Oligschleger [16] developed a procedure to de-mix the quasi-localized eigenstates into a size-dependent propagating part and a size-independent localized part, finding that it is the latter which is predominantly responsible for the enhancement of the number of low frequency states (relative to the continuum level) and thus responsible for the existence of the Boson-peak. Through the calculation of the dynamical structure factor for a minimum $\boldsymbol{k}$-vector accessible to the system, reference [16] also demonstrated that the Ioffe-Regel limit is reached at the numerically evaluated Boson-peak frequency of the system considered. Moreover, after the de-mixing procedure, the corresponding dynamical structure factor of the propagating part narrows. Since only the dynamical structure factor, as seen by Brillouin scattering was calculated, no conclusion in that work was made concerning the polarization of the most affected mode. Subsequent simulation did, however, show that such quasi-localized states are transverse in nature, coupling predominantly to the transverse acoustic modes [17–19].

A connection between the existence of such vibrational modes and the underlying structure of a glass was considered in a series of papers on model two- and three-dimensional atomistic systems [20–22]. In these works, elastic heterogeneity was investigated via the non-affine response of an atomistic system to a global strain, and it was found that only above a certain length-scale self averaging is sufficient to allow for a classical continumm elastic discription of the glassy medium. The vibrational frequency associated with this length-scale was found to correlate well with the location of the Boson peak, suggesting that the contributing vibrational modes are intimately related to the non-affine displacement regime. Importantly, it was the transverse vibrational modes that strongly coupled to the non-affine displacements, which where found to be predominantly solenoidal like and therefore associated with localized shearing. This result provides a concrete connection between local structure and the spatial extent of the anomalous low frequency mode.

Following these works, Shintani and Tanaka [23] have preformed extensive large-scale finite temperature molecular dynamics simulations of model two- and three-dimensional glass systems from which they directly calculated the polarization resolved dynamical structure factors derived from current-current correlation functions. In their work, clear numerical evidence was given that the Boson-peak frequency corresponds to the Ioffe-Regel frequency for the transverse modes and that the longitudinal mode is less affected by the disorder, extending well into the vibrational frequency range of their observed Boson-peak region, and therefore having a higher Ioffe-Regel frequency than Ω_{BP}. This result was achieved for a variety of atomic interactions, one of which involved an angular dependent interaction whose contribution could be connected to the fragility of the model system. They found that with increasing fragility (a decreasing angular-interaction contribution), the Boson-peak reduced in magnitude, demonstrating that for systems such as bulk metallic glasses (BMG), where bonding is primarily scalar and dispersive (not strongly angular), the Boson-peak and its associated effects are at a much reduced intensity, but nevertheless present. These authors also found a correlation between the local atomic density and the strength of the local Boson peak derived from the local VDOS.

Perfoming molecular dynamics simulations of very large model glass systems, Monaco and Mossa [24] investigated the dispersion properties of the accoustic branches for frequencies an order of magnitude lower than that of the Boson peak regime. They observed non-linear dispersion behaviour for both the transverse and longitudinal polarization modes, in which the phase velocity exhibited a minimum at their identified Boson peak frequency, resulting in softening that naturally leads to an enhancement of the vibrational density of states. Their simulations also established that at frequencies below the Boson peak, the broadening is proportional to ω^4 suggesting strong Rayleigh scattering is at play. At and above the Boson peak the broadening changes to an ω^2 dependence, where the Ioffe-Regel limit is reached at the Boson peak frequency for the transverse polarization modes, and at a somewhat higher frequency for the longitudinal mode.

A number of avenues have been undertaken to develop a theoretical understanding of these anomalous vibrational modes and how they might relate to glass structure, driven partly by inelastic scattering experiments and partly by atomistic simulations. For example,

Schirmacher [25] has developed a field theoretic continuum model in which the vibrational dynamics is based on the random spatial variation of the shear modulus, allowing for a prediction of the dispersion and broadening properties of the (Brillouin) dynamical structure factor [26]. A different approach has involved the study of the secular equation for model interacting harmonic oscillators on a regular lattice with spring constant disorder. For example, Taraskin et al. [27] applied effective medium theory to such models to study the VDOS of bulk systems, demonstrating that the Boson-peak may be associated with the lowest van Hove singularity of the reference crystalline system shifting to the low frequency regime – the Boson-peak is the direct result of a considerable decrease in the phonon frequency at which the acoustic branches terminate. Numerical diagonalization of such systems as a function of spring constant disorder demonstrated that particular distributions of spring constant values (when the probability of having a small or negative value is non-zero) can lead to a Boson-peak [28,29]. Such work, which falls into the category of random matrix models, has its historical origins in the very early work of Dyson, who considered the VDOS for one dimensional model systems [30]. It is, however, difficult to reconcile the observed universality seen in the experimental Boson peak with such results which are quite dependent on the choice of spring constant distribution. Additionally, such work does not generally include explicit topological disorder, and therefore direct comparison of these simplified systems to real structural glass is difficult.

Perhaps one of the most well known microscopic models that is able to predict an analytical form of the Boson-peak in the VDOS is that of references [31–33], which formally defines a description of the so-called quasi-localized vibrational modes. The underlying idea is that within the potential energy landscape, there exist local harmonic oscillators that interact bi-linearly with each other to form a new harmonic minimum that is stabilized by anharmonicity, resulting in a renormalized VDOS exhibiting the Boson-peak feature. Importantly, the origin and the shape of the VDOS of the localized harmonic oscillators is not of relevance, whether it may be due to libration as in the case of network glasses, or due to intrinsic disorder as in the case of fragile BMGs, resulting in a distribution of states that is vibrationally universal. This model is found to compare favourably with both neutron and X-ray inelastic scattering data for a wide range of structural glasses [8].

In this paper, these aspects are further investigated by numerical diagonalisation of the Hessian (force matrix) derived from computer generated three-dimensional binary amorphous systems, using a well known model Lennard-Jones potential [34]. The use of a Lennard-Jones interatomic force description is extensive [15,20,21,23,24,35–37] and indeed has been used most recently to investigate the applicability of rigidity theory (primarily used in network glasses) to central-force-based model glasses [38]. In the present work, both $\boldsymbol{k} = 0$ and $\boldsymbol{k} \neq 0$ values of the force matrix are considered, allowing for the calculation of the phonon dispersion curves admitted by an infinite array of unit cells derived from atomisitic simulation, and also the corresponding full dynamical structure factor. Despite such dispersion curves being an artifact of the finite size of the simulation cell, the calculation of $\boldsymbol{k} \neq 0$ provides additional information on the origin of the usually calculated $\boldsymbol{k} = 0$, in terms of how the transverse and longitudinal accoustic branches affect their corresponding eigenvector structure and what role atomic structure might play. In particular, the nature of the resulting eigen-modes are investigated in terms of local atomic quantities, such as local atomic volume, coordination, hydrostatic pressure and the local atomic elastic constants. Here, the elastic stiffness properties are investigated in terms of the eigen-shear moduli derived from the Kelvin form of the elastic stiffness matrix [39]. In Section 2, the atomistic simulation methods, normal mode calculation and local atomic structural analysis methods are briefly introduced. In Section 3 the local atomic properties of the generated structures are fully analysed and the core results of the numerical diagonalisation of the Hessian are given, and their connection with the evaluated local atomic properties is investigated.

It is found that the quasi-local vibrational modes that underlie the Boson peak structure of the vibrational density of states originate from vibrational modes whose spatial environment correlates somewhat with regions of increased free volume and tensile hydrostatic pressure (as seen in Ref. [23]). The correlation is, however, found to be strongest with atomistic environments characterized by significantly reduced local elastic shear moduli. In Section 4, these findings are then directly related to the long-range off-diagonal structure of the underlying Hessian, which is found to be responsible for both the local soft elastic shear moduli and the low frequency localized vibrational modes, leading to the quasi-local eigenstates responsible for the low frequency Boson-peak structure for the used Lennard-Jones potential.

2 Methodology

2.1 Atomistic simulation

For the present work a model (1 : 1) binary Lennard-Jones (LJ) glass is employed:

$$V_{LJ}(r) = 4\varepsilon\left[\left(\frac{\sigma}{r}\right)^{12} - \left(\frac{\sigma}{r}\right)^{6}\right], \tag{1}$$

using the Wahnström parametrization [34]: $\varepsilon = 1$, and $\sigma_{11} = 1$, $\sigma_{12} = \sigma_{21} = 11/12$ and $\sigma_{22} = 5/6$. The potential is cut-off at $r_c = 2.5\sigma$. The masses of the LJ particles are taken as $m_1 = 2$ and $m_2 = 1$. Following standard practice when using such model LJ potentials, all simulation results are reported in dimensionless units, where energy is measured in ε, length in $\sigma_{11} = \sigma$, temperature in ε/k_b, and time in $\tau = (m_1\sigma_{11}^2/\varepsilon)^{1/2} = (m\sigma^2/\varepsilon)^{1/2}$.

Amorphous samples were produced by first generating a well-equilibrated liquid configuration at temperature $T_i = 10\,000 \times k_b$ $[\varepsilon/k_b]$ and hydrostatic pressure

Table 1. Sample names with respect to size, quench rate and final cell dimensions.

Sample name	Atom number	Quench rate	$L_x(\sigma_{11})$	$L_y(\sigma_{11})$	$L_z(\sigma_{11})$
Sample 0a	1728	η_1	11.29	11.32	10.48
Sample 0b	1728	η_2	11.18	11.45	10.42
Sample 0c	1728	η_3	10.71	11.86	10.48
Sample 0d	1728	η_4	13.69	10.03	9.65
Sample 1a	13 824	η_1	22.27	21.95	21.91
Sample 1b	13 824	η_2	21.97	22.20	21.89
Sample 1c	13 824	η_3	21.85	22.39	21.74
Sample 2a	110 592	η_1	44.13	44.11	44.00
Sample 2b	110 592	η_2	44.03	44.03	44.05
Sample 2c	110 592	η_3	43.89	44.10	43.97

$p_i = 8/160\ [\varepsilon/\sigma_{11}^3]$. These structures were then quenched by step-wise reducing both the temperature ($\Delta T = -198.0\, k_b\ [\varepsilon/k_b]$) and pressure ($\Delta p = -0.158/160\ [\varepsilon/\sigma_{11}^3]$) at a given time interval and thereby defining a given quench rate. Four quench rates were considered, corresponding to $\eta_1 = 24.57/500$, $\eta_2 = 24.57/5000$, $\eta_3 = 24.57/50\,000$ and $\eta_4 = 24.57/500\,000\ [\varepsilon/(k_b\tau)]$. For the MD simulations a Parinello-Rahman [40] baro-stat was used to evolve the periodic cell side lengths' response according to the applied hydrostatic pressure and an Anderson-Hoover [41] thermostat was used for temperature control. The baro-stat was constrained to an orthorhombic geometry. Three samples are presently considered containing 1728, 13 824, and 110 592 atoms. Subsequent to the quenching procedure, the samples, now at a temperature $T_f = 100 \times k_b\ [\varepsilon/k_b]$ and pressure $p_f = 0.1/160\ [\varepsilon/\sigma_{11}^3]$, were relaxed to 0 K and zero hydrostatic pressure via molecular statics, applied to both the atomic coordinates and the simulation cell side-lengths using the Parrinello-Rahman method. T_f is approximately one fiftieth of the system's glass transition temperature. Table 1 collects some of the properties of the samples and also defines the naming convention used throughout the present work.

2.2 Normal mode analysis

The fully relaxed samples of the previous section have N atoms, an orthorhombic volume equal to $L_xL_yL_z$, and and an energy equal to $E_0\left(\boldsymbol{R}_1, \cdots, \boldsymbol{R}_N\right)$ evaluated under periodic boundary conditions, where $\boldsymbol{R}_i$ is the position vector of the ith atom. To investigate the vibrational properties of the infinite system constructed by an array of N' such ortho-rhombic unit cells ($N' \to \infty$), the total energy with respect to a variation of the $N' \times N$ independent infinitesimal atomic displacement vectors $\boldsymbol{u}_{i,I}$ can be formally written as $E\left(\{\boldsymbol{R}_{i,I} + \boldsymbol{u}_{i,I}\}\right)$ with I indexing the unit-cell and ranging between 1 and N', i indexing each atom within the Ith unit-cell and ranging between 1 and N, and where $\boldsymbol{R}_{i,I} = \boldsymbol{R}_i + \Delta\boldsymbol{R}_I$. Here $\Delta\boldsymbol{R}_I$ is the position of the Ith unit cell and is given by $\Delta\boldsymbol{R}_I = (n_xL_x, n_yL_y, n_zL_z)$ with $\{n_x, n_y, n_z\} \in$ Integers.

To second order in $\boldsymbol{u}_{i,I}$, $E\left(\{\boldsymbol{R}_{i,I} + \boldsymbol{u}_{i,I}\}\right) = E\left(\{\boldsymbol{u}_{i,I}\}\right)$ can be explicitly written as

$$E\left(\{\boldsymbol{u}_{i,I}\}\right) \approx N'E_0\left(\boldsymbol{R}_1, \cdots, \boldsymbol{R}_N\right) + \frac{1}{2} \sum_{I,J=1,N';i,j=1,N;\mu,\nu=1,3} u_{i,I}^{\mu} \Delta_{i,I;j,J}^{\mu\nu} u_{j,J}^{\nu} \tag{2}$$

where the Greek indices index the polarization directions and

$$\Delta_{i,0;j,0}^{\mu\nu} = \Delta_{ij}^{\mu\nu} = \frac{\partial^2 E_0\left(\boldsymbol{R}_1, \cdots, \boldsymbol{R}_N\right)}{\partial R_i^{\mu} \partial R_j^{\nu}} \tag{3}$$

from which $\Delta_{i,I;j,J}^{\mu\nu}$ may be easily constructed by the appropriate use of neighbouring images of the unit cell.

In terms of a general pair interaction, $V(r)$, equation (3) may be written as

$$\Delta_{ij}^{\mu\nu} = \sum_{a,a\neq i} H_{ia}^{\mu\nu}\delta_{ij} - H_{ij}^{\mu\nu}\left(1 - \delta_{ij}\right), \tag{4}$$

where

$$H_{ij}^{\mu\nu} = \left[V''\left(R_{ij}\right) - \frac{V'\left(R_{ij}\right)}{R_{ij}}\right] \frac{R_{ij}^{\mu} R_{ij}^{\nu}}{R_{ij}^2} + \frac{V'\left(R_{ij}\right)}{R_{ij}} \delta^{\mu\nu}. \tag{5}$$

In equation (4), the first term gives the 3×3 block diagonal elements and the second term the off-diagonal block elements, which can be seen as the effective spring constants of the system. In the above equations, the δ represents the Kroneck-delta in the associated indices.

Due to translational symmetry with respect to the unit cell coordinates, $\Delta\boldsymbol{R}_I$, a corresponding reciprocal space can be defined and the Hessian $\Delta_{i,I;j,J}^{\mu\nu}$ may be diagonalized with respect to I and J, transforming equation (2) to

$$E\left(\{\boldsymbol{u}_i(\boldsymbol{k})\}\right) \approx N'E_0\left(\boldsymbol{R}_1^0, \cdots, \boldsymbol{R}_N^0\right) + \frac{1}{2} \sum_{i,j=1,N;\mu,\nu=1,3;\boldsymbol{k}\in 1\text{stBZ}} u_i^{\mu}(\boldsymbol{k}) \Delta_{i,j}^{\mu\nu}(\boldsymbol{k}) u_j^{\nu}(\boldsymbol{k}) \tag{6}$$

where the irreducible Hessian is

$$\Delta_{ij}^{\mu\nu}(\boldsymbol{k}) = \sum_{IJ} \Delta_{i,I;j,J}^{\mu\nu} \exp(i\boldsymbol{k} \cdot (\boldsymbol{R}_I - \boldsymbol{R}_J)), \tag{7}$$

and the wavevector, $\boldsymbol{k}$, spans the range of the first Brillouin zone: $(\pm\pi/L_x, \pm\pi/L_y, \pm\pi/L_z)$.

The normal modes of the infinite system may then be obtained by the solution of the eigenvalue equation,

$$\sum_{j\nu} \left(m_i \left[\omega_n(\boldsymbol{k})\right]^2 \delta_{ij}\delta^{\mu\nu} - \Delta_{ij}^{\mu\nu}(\boldsymbol{k})\right) u_{j,n}^{\nu}(\boldsymbol{k}) = 0 \tag{8}$$

where m_i is the atomic mass of the ith atom. For each of the N' reciprocal space vectors, $\boldsymbol{k}$, there exists $3N$ eigenstates, $u_{j,n}^{\nu}(\boldsymbol{k})$ with eigenfrequency $\omega_n(\boldsymbol{k})$ ($n = 1, \ldots, 3N$). It is these normal modes that will be

used to investigate the vibrational properties of the samples produced in the previous section[1]. It is noted that the eigenstate, $u^{\nu}_{j,n}(\boldsymbol{k})$ for any non-zero value of $\boldsymbol{k}$, has the same physical standing as the $\boldsymbol{k}=0$ eigen-state calculated in past work [12–14]. Indeed $u^{\nu}_{j,n}(\boldsymbol{k}=0)$ corresponds to what has been calculated in these past works.

From the resulting eigen-frequencies, $\omega_n(\boldsymbol{k})$, the VDOS with respect to the phonon frequency, ω, may be calculated:

$$\rho(\omega) = \sum_n \frac{V}{(2\pi)^3}\int_{1^{st}BZ} d^3\boldsymbol{k}\delta\left(\omega-\omega_n(\boldsymbol{k})\right) \approx \sum_n \delta\left(\omega-\omega_n(\boldsymbol{k}=0)\right), \tag{9}$$

where the last step is a good approximation when N is large and only the overall shape of the VDOS is of interest. For a detailed investigation of the Boson-peak region, particularly when it has a weak signature (as in the present work), the full Brillouin zone integration is used. Indeed, it is noted that in using equation (1) as a model for cohesion, the concentration of low frequency modes is expected to be low compared to that when using the soft sphere glass cohesion model [13]. Diagonalization of the Hermitian matrix generated via equations (3) and (7) is performed either via the Intel MKL-Lapack routines[2] or the Arnoldi package [42].

The number of atoms participating in a particular eigenstate, $u^{\nu}_{j,n}(\boldsymbol{k})$, may be obtained via the participation number [43]

$$\mathrm{PN}_n(\boldsymbol{k}) = \left[\sum_i \left|\boldsymbol{u}_{i,n}(\boldsymbol{k})\right|^4\right]^{-1}, \tag{10}$$

where $\boldsymbol{u}_{i,n}(\boldsymbol{k})$ is the three-dimensional polarization vector of atom i for the mode $(n,\boldsymbol{k})$. Assuming a normalized eigenvector, $\mathrm{PN}_n(\boldsymbol{k})$ will thus range between unity (when the eigenstate is concentrated on just one atom) and N (when the eigenstate is distributed evenly over the entire sample). The participation ratio, defined as $PN_n(\boldsymbol{k})/N$, is also often used when comparing samples of different sizes, since for certain eigenstates the fractional value can be insensitive to the effects of box-normalisation and therefore the size of the employed simulation cell. The participation number/ratio has been used extensively in the normal mode study of the vibrational modes of glasses [13–15]. It is emphasized that the participation number/ratio gives information about which atoms contribute to the eigenstate, however, it having a low value does not consitute evidence that the eigen-state is localized. Localization can only be formally established if the participation ratio approaches zero in the bulk limit. Since the participation number/ratio effectively identifies those atoms which are involved in the particular oscillation mode, it may be used to define a characteristic local environment seen by the entire eigen-mode, by constructing the participation-number-weighted (PNW) average for any local atomic quantity X_i:

$$\langle X\rangle_{n,\boldsymbol{k}} = \sum_i X_i \left|\boldsymbol{u}_{i,n}(\boldsymbol{k})\right|^4 / \sum_i \left|\boldsymbol{u}_{i,n}(\boldsymbol{k})\right|^4. \tag{11}$$

To investigate sound propagation, the longitudinal and transverse dynamical structure factors may be easily derived from the overlap of each mode with a plane wave of the appropriate polarization [23]. Specifically,

$$S_L(\boldsymbol{q},\omega) \sim \frac{q^2}{\omega^2}\sum_n \left|\sum_i \left[\boldsymbol{u}_{n,i}(\boldsymbol{q})\cdot\boldsymbol{q}\right]\exp\left(i\boldsymbol{q}\cdot\boldsymbol{r}_i\right)\right|^2 \delta(\omega-\omega_n) \tag{12}$$

and

$$S_T(\boldsymbol{q},\omega) \sim \frac{q^2}{\omega^2}\sum_n \left|\sum_i \left[\boldsymbol{u}_{n,i}(\boldsymbol{q})\times\boldsymbol{q}\right]\exp\left(i\boldsymbol{q}\cdot\boldsymbol{r}_i\right)\right|^2 \delta(\omega-\omega_n). \tag{13}$$

As discussed in Section 1, the dynamical structure factor is an important quantity since the longitudinal component is experimentally accessible via neutron and X-ray inelastic scattering.

2.3 Local atomic properties

For a pair-potential, $V(r)$, the global stress tensor may be calculated via

$$\sigma^{\mu\nu} = \frac{1}{2V}\sum_{ij} V'\left(R_{ij}\right)\frac{R^{\mu}_{ij}R^{\nu}_{ij}}{R_{ij}} \tag{14}$$

and the global elastic stiffness tensor via

$$C^{\mu\nu\alpha\beta} = \frac{1}{2V}\sum_{ij}\left[V''\left(R_{ij}\right)-\frac{V'\left(R_{ij}\right)}{R_{ij}}\right]\frac{R^{\mu}_{ij}R^{\nu}_{ij}R^{\alpha}_{ij}R^{\beta}_{ij}}{R^2_{ij}} + \sigma^{\nu\beta}\delta_{\mu\alpha}+\sigma^{\nu\alpha}\delta_{\mu\beta}. \tag{15}$$

Here, in both cases, V is the volume of the simulation cell. It is noted that for a system under zero external stress, the last two terms in equation (15) are equal to zero. To correctly determine the contributions arising from one or more atoms, thereby defining either a local stress or elastic constant matrix, the individual bond contributions in equations (14) and (15) must be appropriately weighted [44,45]. Given a volume element labeled as a and any two atoms i and j, and drawing a line between these two atoms resulting in a length R_{ij}, the weight of that bond to the chosen element is $\Lambda_{a,ij}=\Delta_a R_{ij}/R_{ij}$, where $\Delta_a R_{ij}$ is the total line length of R_{ij} that lies within the volume element a. The resulting local stress and elastic stiffness tensors are

$$\sigma^{\mu\nu}_a = \frac{1}{2V_a}\sum_{ij} V'\left(R_{ij}\right)\frac{R^{\mu}_{ij}R^{\nu}_{ij}}{R_{ij}}\Lambda_{a,ij} \tag{16}$$

[1] As is normally the case, the dynamical matrix divided by a $\sqrt{m_i m_j}$ term is, in fact, diagonalised yielding the eigenstates u'^{μ}_i, from which the true eigen-states are reconstructed via $u^{\mu}_i = u'^{\mu}_i/\sqrt{m_i}$.

[2] Intel. Intel Math Kernel Library (Intel MKL) 10.2, available: http://software.intel.com/en-us/intel-mkl/.

and

$$C_a^{\mu\nu\alpha\beta} = \frac{1}{2V_a}\sum_{ij}\left[V''(R_{ij}) - \frac{V'(R_{ij})}{R_{ij}}\right] \times \frac{R_{ij}^{\mu}R_{ij}^{\nu}R_{ij}^{\alpha}R_{ij}^{\beta}}{R_{ij}^2}\Lambda_{a,ij} + \sigma_a^{\nu\beta}\delta_{\mu\alpha} + \sigma_a^{\nu\alpha}\delta_{\mu\beta}, \quad (17)$$

where V_a is the volume of the chosen ath volume element. In the above, for heterogeneous atomic configurations, $\sigma_a^{\mu\nu}$ is generally not zero when the global stress is zero. It is noted that in equations (14) and (15), atoms i and j do not need to lie within the volume V_a to contribute to the stress or elastic tensor for that particular volume element. In the present work, volume partitioning is performed at the atomic level via a Voronoi tessellation using the voro++ package [46] to obtain a measure of the non-overlapping local atomic volume of each atom in the simulation cell.

Equation (15) is referred to as the Born contribution to the elastic constants and represents the elastic stiffeness corresponding to a purely affine distortion of the atomic system. Previous work has however shown that for glassy systems there is a significant non-affine component that contributes to the elastic constants [21,22,35] and therefore a considerable part of the elastic energy. Thus at zero Kelvin, equation (15) will give an over-estimation of the experimentally determined elastic constants. Whilst it is possible to directly calculate this global contribution via the inverse of the dynamical matrix [44], the present work will instead investigate the effect on of the non-affine component on both the bulk modulus and the isotropic shear modulus via the systems energy dependence as a function of a finite simulation cell distortion. Following [21], an appropriate affine transformation is applied to the periodic simulation cell, and for each value of the corresponding distortion parameter γ, the atomic coordinates are relaxed using the conjugate gradient method. To obtain the bulk modulus (K) an isotropic volume change is needed and is given by the strain transformation matrix,

$$\begin{pmatrix} 1 & 0 & 0 \\ 0 & 1 & 0 \\ 0 & 0 & 1 \end{pmatrix}\gamma, \quad (18)$$

which, according to linear elasticity, will give an energy dependence $9/3K\gamma^2$. To obtain the isotropic shear modulus (μ), the strain transformation matrix,

$$\begin{pmatrix} 1 & 0 & 0 \\ 0 & -\frac{1}{2} & 0 \\ 0 & 0 & -\frac{1}{2} \end{pmatrix}\gamma, \quad (19)$$

is used with the corresponding elastic energy equalling $9/3\mu\gamma^2$.

Despite the inadequacy of the Born term to describe the elasticity of an amorphous system, the corresponding local definitions of the Born elastic modulii (Eqs. (16) and (17)) offer useful information on the local environment of each atomic in terms of the higher derivatives of the crystal potential, and it will be these terms that will be used in subsequent sections.

For a more lucid characterization of the local elastic moduli the 6×6 Kelvin matrix notation [39] is used rather than the more usual Voigt matrix notation, since the former reduction results in a stress-strain relation that retains its tensorial nature. This has the benefit that the resulting elastic stiffness matrix may be diagonalised to obtain the dilation modulus and the five independent eigen-shear modes. In terms of a Voigt elastic stiffness matrix $C_{\alpha\beta}^V$ the corresponding Kelvin elastic stiffness (tensor) matrix is

$$C_K^{\mu\nu} = A^{\mu\nu}C_V^{\mu\nu}, \quad (20)$$

where

$$\tilde{A} = \begin{pmatrix} 1 & 1 & 1 & \sqrt{2} & \sqrt{2} & \sqrt{2} \\ 1 & 1 & 1 & \sqrt{2} & \sqrt{2} & \sqrt{2} \\ 1 & 1 & 1 & \sqrt{2} & \sqrt{2} & \sqrt{2} \\ \sqrt{2} & \sqrt{2} & \sqrt{2} & 2 & 2 & 2 \\ \sqrt{2} & \sqrt{2} & \sqrt{2} & 2 & 2 & 2 \\ \sqrt{2} & \sqrt{2} & \sqrt{2} & 2 & 2 & 2 \end{pmatrix}. \quad (21)$$

The dilation modulus is equal to three times the bulk modulus, and the five eigen-shear moduli are determined from the eigenvalues of $\tilde{P}^{-1}\cdot\tilde{C}_k\cdot\tilde{P}$, where $\tilde{P}$ projects out volume changes, and is given by

$$\tilde{P} = \begin{pmatrix} \frac{2}{3} & -\frac{1}{3} & -\frac{1}{3} & 0 & 0 & 0 \\ -\frac{1}{3} & \frac{2}{3} & -\frac{1}{3} & 0 & 0 & 0 \\ -\frac{1}{3} & -\frac{1}{3} & \frac{2}{3} & 0 & 0 & 0 \\ 0 & 0 & 0 & 1 & 0 & 0 \\ 0 & 0 & 0 & 0 & 1 & 0 \\ 0 & 0 & 0 & 0 & 0 & 1 \end{pmatrix}. \quad (22)$$

For a perfectly isotropic environment, all five Kelvin eigen-shears will be equal to 2μ (where μ is the usual isotropic shear modulus).

The Kelvin elastic stiffness matrix has been most recently applied to the investigation of connectivity of elastic heterogeneity at finite temperature in model metallic glasses and its relation to structural stability [47]. This work has shown that when the appropriate thermal contribution to the local elastic moduli is included, within the typical atomistic timescale, the temperature at which percolation of negative local eigen-shears occurs (leading to global mechanical failure) correlates well with the system's glass transition temperature.

3 Results

3.1 Local structure analysis

Figure 1 displays some global properties of the fully relaxed structures as a function of the logarithm of the inverse quench rate for all three sample sizes. Figures 1a and 1b show respectively that the average energy and average volume per atom decrease linearly with respect to the logarithm of the inverse quench rate. On the other

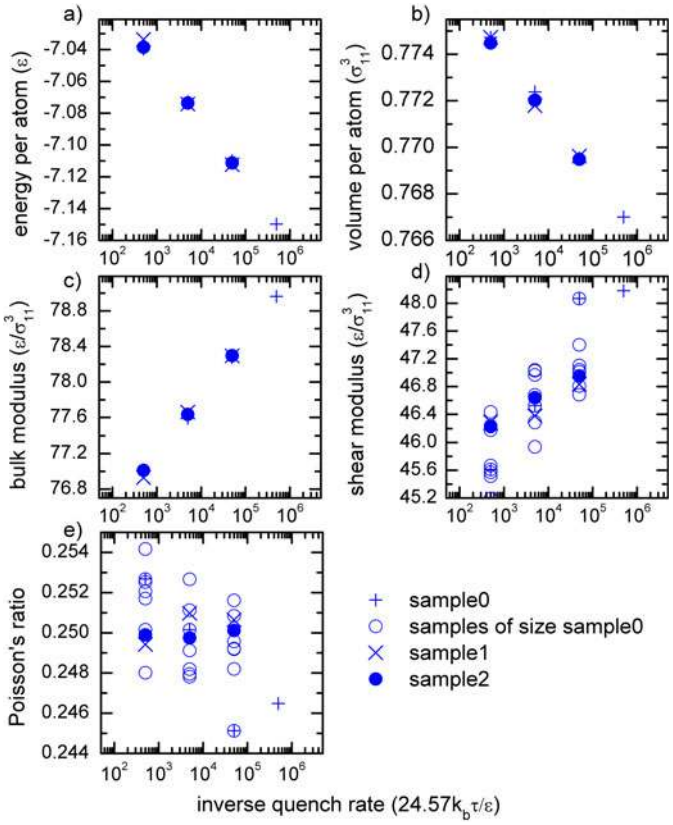

Fig. 1. (Color online) (a) Average energy per atom, (b) average volume per atom, (c) global bulk modulus, (d) global isotropic shear modulus, and (e) global Poisson's ratio as a function of inverse quench rate and sample size. In (d) and (e) data is also shown from six sample realizations of similar size to sample 0.

hand, the global bulk modulus (Fig. 1c) and global shear modulus (Fig. 1d) both increase. For the case of the global shear modulus significantly more scatter is evident, which reduces with increasing sample size. The rate of increase of these two moduli is comparable, resulting in little change in the global Poisson ratio (see Fig. 1e). This is particularly the case for sample 2, which has an almost constant Poisson ratio as a function of inverse quench rate due to the significantly less scatter in sample 2's global shear modulus. Thus the Poisson ratio, as calculated via equation (15), appears not to be so sensitive to the degree of structural relaxation. To gain quantitative insight in the degree of scatter in the shear modulus (and therefore Poisson ratio) Figures 1d and 1e also display data coming from six realizations similar in size to sample 0 for the first three quench rates. Despite the scatter in Figure 1d, a clear increase in the shear modulus with respect to decreasing quench rate is evident. The scatter also appears to be insensitive to the actual quench rate suggesting its origin lies in a fundamental heterogeneity at the length scale of sample 0, which can be well averaged at the length scale of sample 2. Since all three quench rates involve precisely the same sample preparation sequence, the horizontal axis of Figure 1 may also be viewed as an effective sample preparation time, and thus the approximately linear decrease in energy and volume per atom indicates a logarithmic slowing down of the relaxation dynamics with respect to the quench rate – an observation which is expected for glassy materials [48]. In summary, reducing the quench rate results in more energetically relaxed samples characterized by a higher number density and higher elastic stiffness moduli.

Table 2. Unrelaxed and relaxed bulk elastic modulii in units of $\varepsilon/(\sigma_{11})^2$, calculated numerically by distorting the simulation cell. The resulting relaxed Poisson ratio is also listed.

Sample	K_{unrel}	μ_{unrel}	K_{rel}	μ_{rel}	ν_{rel}
Sample 0c	77.23	47.04	75.13	21.37	0.37
Sample 0d	77.80	47.80	75.67	23.63	0.36
Sample 1c	77.22	46.24	76.06	19.92	0.38
Sample 2c	77.23	46.42	75.58	20.15	0.38

To investigate the contribution of the expected non-affine contribution to the bulk modulus and isotropic shear modulus, the procedure associated with equations (18) and (19) is now used. Table 2 lists the resulting elastic constants for a range of samples, with and without (purely affine) relaxation when γ is varied from -0.001 to 0.001. Such a small range of γ ensures that no irreversible structural transformation occurs. It is seen that without relaxation the elastic constants differ little from those explicitly calculated using equation (17). However when structural relaxation is allowed, the bulk modulus decreases only slightly, whereas the shear modulus is reduced by more than half resulting in a significant increase in the Poisson ratio. This result was also found in the work of [21] and is a signature that the non-affine component is mainly associated with shear deformations.

Figure 2 now displays the distribution of local atomic quantities for sample 0, for all four quench rates considered. In all panels, the vertical red line indicates the corresponding global quantity taken from Figure 1 where for the case of (e) (the Kelvin eigen-shears), the appropriate quantity is by definition twice the isotropic shear modulus. Figures 2a and 2b show the distribution of the local energy and local Voronoi volume. A two-peak structure is clearly evident in both figures reflecting the two atom types of the LJ interaction, where in the case of the local atomic energy (Fig. 2a), the left-most peak corresponds to atoms of type '1' and the right-most to atoms of type '2'. For the case of local Voronoi volume, the left-most peak in Figure 2a corresponds to atoms of type '2' and the right-most to atoms of type '1'; see also Figure 3b. Thus atoms of type '2' generally exist in regions of reduced Voronoi volume when compared to the globally averaged volume per atom. The twin-peak structure of the Voronoi volume may be qualitatively rationalized by the fact that for atoms of type '1', $\sigma_{11} = 1$, and for atoms of type '2', $\sigma_{22} = 5/6$. Thus the LJ potential of atoms of type '1' is more extended in range than that of type '2', in particular at the inner region of the potential, leading to an expected larger local Voronoi volume.

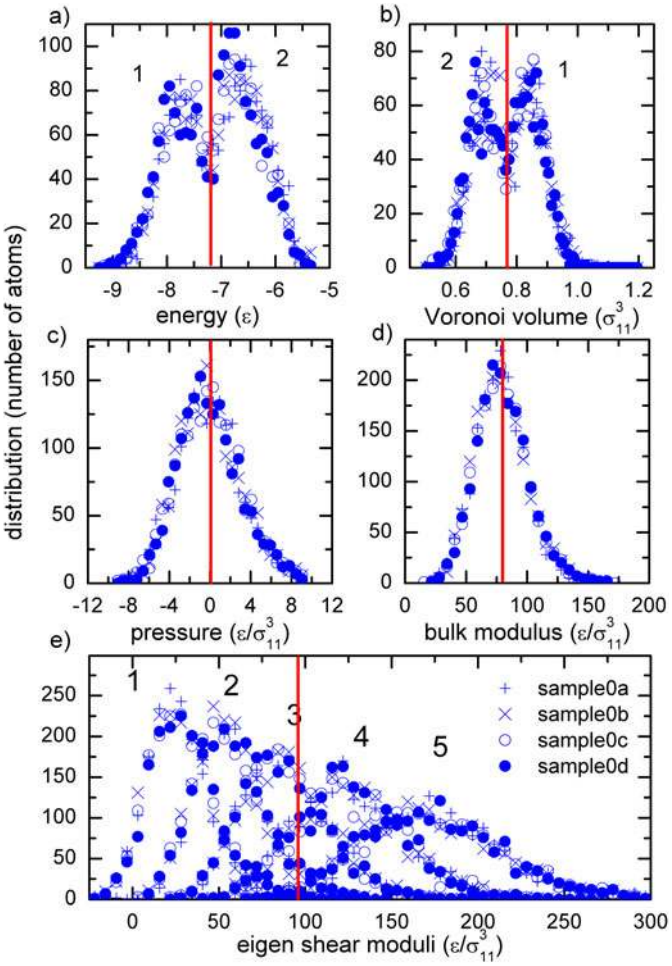

Fig. 2. (Color online) Distribution of local (a) energy, (b) Voronoi volume, (c) hydrostatic pressure, (d) bulk modulus, and (e) the five eigen-shear moduli in ascending order for sample 0 for the four different quench rates. In (a) and (b) the dual peak structure arises from single peak distributions of the indicated atom type.

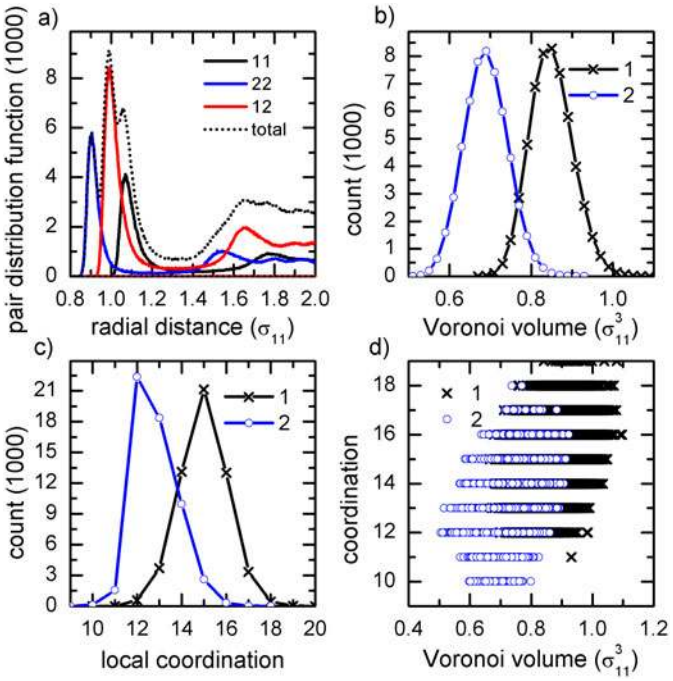

Fig. 3. (Color online) Atom type resolved (a) pair distribution function, (b) Voronoi volume distribution, (c) local coordination distribution, and (d) local coordination-Voronoi scatter graph for sample 2c.

No such twin-peak structure can be visually resolved in the distribution of the local hydrostatic pressure (Fig. 2c), local bulk modulus (Fig. 2d), and the local eigen-shears (Fig. 2e, which displays the distributions for all five local eigen-shear moduli). Figure 2e shows that the three lowest local eigen-shears are considerably smaller than the global shear modulus (Fig. 1d), where for the lowest eigen-shear a certain proportion is negative. General inspection of Figure 2 shows that the distributions vary little as a function of quench rate, indicating that the global variations in these quantities seen in Figure 1 are quite small when compared to the standard-deviations of the corresponding local quantities. The extremely broad range of eigen-shear moduli seen in Figure 2e is the origin of the increased scatter of the global elastic shear modulus seen in Figure 1d, where it is only in the largest sample that a distinctly smooth trend of increasing shear modulus is seen as a function of inverse quench rate.

For sample 0d, when the hydrostatic pressure and elastic moduli distributions are 'type' resolved, it is found that two quite similar distributions appear which are shifted relative to each other, although the significant scatter in the distributions prevents a statistically meaningful quantitative analysis. However, for the case of sample 2c, where there is significantly less scatter in the derived distributions (not shown), quantitative differences become evident. For the case of the local hydrostatic pressure, the type resolved single peak distributions are identical in shape but shifted relative to each other, such that the global average hydrostatic pressure of atoms of type '2' is negative (tensile) and for atoms of type '1' is positive (compression). These amounts are approximately 20% of the standard deviation of the distribution and add to approximately zero giving a total hydrostatic pressure of approximately zero. The differences in type resolved pressure are, however, small since no double hump structure is evident, as seen in Figures 2a and 2b for the local energy and Voronoi volume. For the type resolved local bulk modulus distributions no statistical meaningful difference in the distributions could be determined. However for the local eigen-shear modulus, the type resolved distributions indicate that the distributions for type '2' atoms are shifted to lower values to the extent that the majority of negative local lowest eigen-shear modulus values arise from atoms of type '2'.

Figure 3a displays the pair distribution function for sample 2c, where the individual contributions from type '11', type '22' and type '12' bonds are also shown. Its form is in agreement with previous work using the same LJ potential [49]. Inspection of this figure reveals a well-defined coordination shell regime ($r < 1.4\sigma$) with a three-peak

structure that is a direct result of atom type resolved contributions, where on average atoms of type '2' are closer together than atoms of type '1', and intermediate bond distances exist primarily between atoms of different type. This finding is responsible for the two-peak structure seen in the distribution of Voronoi volume (Fig. 2b) for sample 0d, where Figure 3b now displays the corresponding type resolved Voronoi volume distributions for sample 2c. The mean local Voronoi volume for type '1' atoms is $0.85\sigma^3$ and for type '2' atoms it is $0.69\sigma^3$. Insight into how local structure can facilitate such a result may be gained by investigating the type resolved coordination number, where the latter has been calculated by counting the number of faces per atom in the atomic-scale Voronoi construction. This measure of coordination was found to be similar to simply counting the number of neighbours that are within a radial distance defined here to be $r < 1.4\sigma$. Figure 3c displays the type resolved coordination distributions, showing that atoms of type '2' have a lower coordination than atoms of type '1'. The average coordination for type '1' atoms is ≈15.1 and for type '2' atoms is ≈12.8, and the combined average is 13.9. Thus the smaller local Voronoi volumes of type '2' atoms are accommodated by a smaller coordination number and the larger local Voronoi volumes of type '1' atoms are accommodated by a correspondingly larger one. Such an accommodation mechanism tends to minimize fluctuations in local atomic density. Figure 3d shows a scatter-plot between coordination and Voronoi volume for both types of atoms, and it is observed that within each type resolved distribution a similar trend is seen: those atoms with a smaller coordination generally have a smaller local Voronoi volume. Similar results are obtainable for the smaller samples.

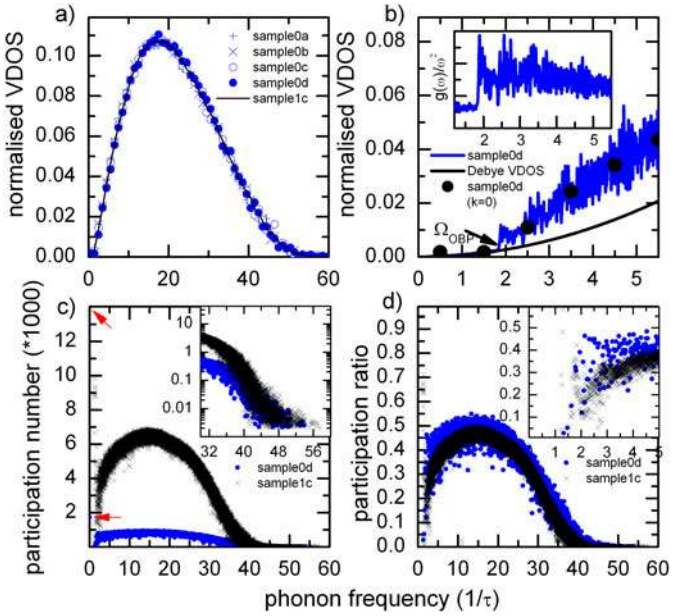

Fig. 4. (Color online) (a) Vibrational density of states for different quench rates and sample sizes, calculated via binning of the $\omega_{\boldsymbol{k}=0}$ eigenvalues. (b) Low frequency vibrational density of states for sample 0d, using a first Brillouin zone integration scheme and a simple continuum Debye model that employs the global relaxed elastic constants listed in Table 2. In this figure, the data taken from the $\boldsymbol{k} = 0$ VDOS of (a) is also shown. Inset: plot of sample 0d VDOS divided by the ω^2 (c) Participation number for sample 0d and sample 1c (inset, high-frequency regime plots using a logarithmic scale) and (d) the corresponding participation ratio (inset, low frequency regime). In (c), the red arrows indicate the corresponding three translational zero frequency modes for each sample.

3.2 Vibrational properties

For the detailed analysis of the vibrational properties the most relaxed sample of each simulation cell size is used. Other samples coming from repeated sample production and/or different quench rates exhibited similar properties to what will be presently shown. The insensitivity of the vibrational properties to a particular realization of the disorder produced by use of a Lennard-Jones potential has also been encountered in past work [21].

3.2.1 Phonon density of states and the participation number

Figure 4a displays the vibrational DOS of sample 0d derived from binning the $\boldsymbol{k} = 0$ phonon frequency eigenvalues for the four different quench rates (see Eq. (9)). The VDOS is normalized to the number of states per atom, which is three. Similar data is shown for sample 1, for its slowest quench rate. Inspection of these curves reveals a featureless distribution of states free of the Van Hove singularity structure seen in crystalline systems. The overall form of the VDOS is typical of past work and well described by the universal form suggested in references [36,37]. Such a VDOS is also typical of weakly disordered systems such as grain boundaries in a nanocrystalline network [50–52]. Inspection of Figure 4a reveals that the form of the VDOS at this resolution is not so dependent on the quench rate used and the size of the sample. By using only the $\boldsymbol{k} = 0$ eigenvalues, and dividing by ω^2, it becomes evident that the low frequency structure of the VDOS is not of sufficient detail to reveal the expected Boson-peak structure for the currently employed LJ inter-atomic potential. To gain the needed resolution in the low frequency limit a full Brillouin zone integration is used (Eq. (9)) and Figure 4b displays the resulting VDOS of sample 0d for the low frequency regime. To do this, a regular reciprocal-space mesh over the (orho-rhombic) irreducible Brillouin zone was used to integrate equation (9) in which the frequency delta-function was approximated by a normalized Lorentzian of width of $0.1\sqrt{2}\ 1/\tau$. Also shown is the similarly normalized Debye VDOS,

$$\rho_{\text{Debye}}(\omega) = \frac{1}{2\pi^2}\left(\frac{1}{v_{\text{l}}^3} + \frac{2}{v_{\text{t}}^3}\right)\omega^2, \tag{23}$$

where the longitudinal and transverse sound velocities are given respectively by

$$v_{\mathrm{l}} = \sqrt{\frac{K + \frac{4}{3}\mu}{m_0}} \tag{24}$$

and

$$v_{\mathrm{t}} = \sqrt{\frac{\mu}{m_0}}. \tag{25}$$

Here m_0 is the mass density taken as $m_0 = N(m_1 + m_2)/(2V)$. Equations (24) and (25) are derived using isotropic elasticity, where K is the bulk modulus and μ is the isotropic shear modulus. It was found that the Debye VDOS agrees extremly well with the numerical VDOS when the relaxed elastic constants in Table 2 are used rather than the unrelaxed values or those calculated via equation (17). This result indicates that the structural relaxation occuring during the finite distortion procedure described in Section 3.1 is well described by the Harmonic approximation of the energy (Eq. (2)). Figure 4b reveals an enhancement of states with respect to the Debye level beginning at a frequency $\Omega_{\mathrm{OBP}} \approx 1.9$. Here Ω_{OBP} should not be considered as the frequency of the Boson-peak, but rather as the frequency indicating the onset of the Boson-peak region.

Throughout the remainder of this work, the low frequency band-edge region will refer to the region close to and at Ω_{OBP}. The inset for Figure 4b plots the VDOS in the standard representation of $\rho(\omega)/\omega^2$. Figures 4a and 4b demonstrate that although there exists an enhancement of low frequency modes, the smooth and continuous Boson peak structure seen experimentally will not be obtainable using the present sample sizes with the current LJ potential. This indicates that the present LJ parametrization results in a fragile glass structure, generating a rather weak Boson peak signature, as expected for systems described by pair-wise atomic interactions [23].

To gain insight into the nature of the eigen-modes that lead to the VDOSs seen in Figure 4a, the participation number at $\boldsymbol{k} = 0$ is plotted in Figure 4c for the entire bandwidth of phonon frequencies of sample 0d and sample 1c. The overal form of the curves are similar to that seen in references [14–16]. In the high-phonon-frequency regime the eigenstates involve a considerably reduced number of atoms – between three and several tens of atoms. This feature is independent of sample size (see inset of Fig. 4c, where the participation number is plotted using a logarithmic scale), suggesting that truly localized states exist in this regime. Such localized vibrational states have also been observed in grain-boundary structures, where their location could be correlated with regions of compressive stress and under-coordinated atoms [51,52]. For the current work, in addition to visual inspection of the eigen-modes, the localized nature of the high-frequency states was confirmed by performing a statistical analysis of the phonon frequency separation by investigating the distribution of the frequency intervals between neighbouring eigenvalues. If such states are truly localized then any two states with neighbouring phonon frequency eigenvalues should be uncorrelated and thus the distribution will follow simple Poisson statistics, since spatially any two such states will be on average well separated [53]. This behaviour was indeed confirmed from the high-frequency eigenvalue data in Figures 4c and 4d.

At intermediate phonon frequencies, a clear dependence of the participation number on system size is apparent. However, by dividing the participation number by the number of atoms (to obtain the participation ratio) the two curves fall on top of each other – see Figure 4d. Such a simple volume scaling indicates extended modes that are normalized to the simulation cell. The corresponding participation ratio values in this frequency regime may be rationalized by considering the participation number derived from a normalized plane wave continuum solution: $\phi_n(x) = \sin(2\pi nx/L)/L^{3/2}$, which gives a participation ratio equal to 2/3. Thus in this frequency regime, the participation numbers are slightly less than that expected for a continuum homogeneous model description indicating an underlying heterogeneity of the modes. In terms of a level spacing analysis, references [36,37] have found that for this region of frequencies, the overal fluctuation properties of the VDOS is well described by the Gaussian orthogonal ensemble of random-matrices, rather than by Poisson statistics, indicating that the underlying modes are indeed extended and therefore system size dependent.

At very low frequencies (the Boson-peak regime) the participation number again reduces, indicating modes involving a considerably reduced number of atoms. However, unlike the high-frequency regime, many of these modes do depend on system size as evidenced by the similarity of the participation ratio in this regime, see Figure 4d and its inset, and therefore may also be referred to as extended modes. Finally, for all samples, there exist three zero-frequency modes whose participation numbers are equal to the number of atoms and whose participation ratio is equal to unity. In terms of the participation number, these modes are indicated with red arrows for each sample in Figure 4c and represent the three-dimensional translational invariances ($\boldsymbol{k} = 0$) of the system.

To relate the participation number data seen in Figure 4 to atomic structure, Figures 5 and 6 now display the PNW (Eq. (11)) local atomic properties for sample 1d as a function of the corresponding phonon eigen-frequency, where each eigen-mode has been coloured according to its corresponding participation ratio. Specifically, Figure 5a displays the PNW atom-type, revealing that the high-frequency localized eigenstates mainly consist of atoms of type '2'. On the other hand, at the lower phonon frequency end of the figure, the eigenstates generally consist of both types of atoms with the exception of a few eigenstates at the low frequency band-edge that are dominated by atoms of type '2'. Figures 5b and 5c show respectively the Voronoi volume and coordination as a function of the corresponding phonon eigen-frequency. Both the Voronoi volume and coordination tend to decrease with increasing phonon frequency, a trend that can be largely rationalized by the frequency dependence of the atom type

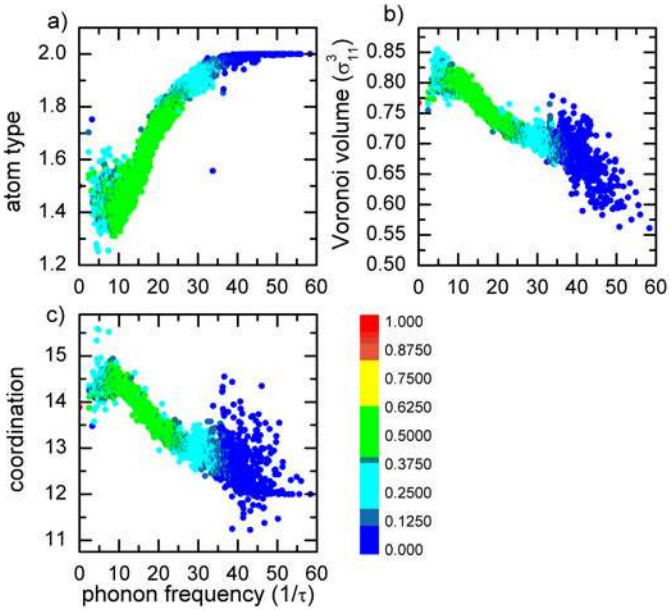

Fig. 5. (Color online) Scatter plots of participation-number-weighted (a) atom-type, (b) local Voronoi volume and (c) local coordination as a function of corresponding phonon eigen-frequency for sample 0d. Data is colour-coded according to the participation ratio for each corresponding mode, see colour bar.

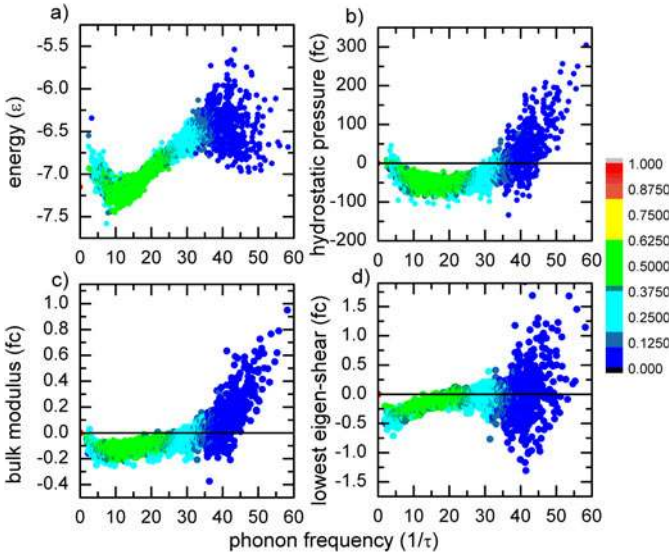

Fig. 6. (Color online) Scatter plots of participation-number-weighted local (a) energy, (b) hydrostatic pressure, (c) bulk modulus, and (d) lowest eigen-shear as a function of corresponding phonon eigen-frequency for sample 0d. The vertical axes in (b) to (d) are plotted as the fractional change (fc) relative to the corresponding globally averaged value. Data is colour-coded according to the participation ratio for each corresponding mode, see colour bar.

(Fig. 5a) and the corresponding distributions of Voronoi volume and coordination seen in Figures 3b and 3c.

Figure 6a now shows the PNW local energy, demonstrating a trend that again can be largely rationalized by the corresponding atom-type behaviour. Figure 6b shows the PNW local hydrostatic pressure revealing that the atomic environment of the high-frequency localized states is generally under a compressive stress. This observation was also made for general grain boundaries in computer generated metallic bulk nanocrystalline systems [51,52] and predicted by theory [54]. Figure 6b further shows that below a certain phonon frequency threshold (less than approximately 35 $(1/\tau)$), the PNW hydrostatic pressure becomes negative indicating that in the region of size-dependent extended modes, the atomic environment seen by the eigenstates is on average under a tensile hydrostatic pressure. At very low phonon frequencies, the PNW hydrostatic pressure becomes less negative eventually approaching the bulk global value of (approximately) zero. It is noted that unlike the case of a regular crystalline lattice, the globally averaged local pressure for such a disordered system will not equal zero, even though the global pressure is zero, since via equation (16) it may be seen that it is the local-volume-weighted average of the local stress which is identical to the global stress of the system, and not simply the direct sum of the local stresses. The globally averaged local pressure is, however, small and it is for this reason that the fractional values in Figure 6b (and also in Fig. 9b of Sect. 3.2.2) are so large.

Figure 6c now plots the fractional change in bulk modulus relative to the bulk global value. In this figure it is seen that the high-frequency eigenstates are generally in regions of higher local bulk modulus, whereas at the lower frequencies the atomic environment is mainly in regions of lower local bulk modulus. Figure 6d displays the fractional change in the PNW lowest eigen-shear (where a value of less than -1.0 indicates a negative modulus). For the high-frequency regime no clear trend is seen, with some eigenstates being in regions of negative eigen-shear. On the other hand, in the lower-frequency regime, in general the eigenstates exist in regions of reduced lowest eigen-shear (by up to 50%).

It is worth mentioning that past work has shown that in three dimensions there exists a non-zero phonon frequency above which the modes exhibit Anderson localization [55], and below which the states constitute extended modes: see for example reference [56] and references therein, and more recently reference [57]. The critical phonon frequency at which this separation occurs is referred to as the phonon mobility edge. The extended states with frequencies below this mobility edge have been referred to as "Extendons" in which those with a frequency less than the characteristic Boson peak frequency are called "Propagons" and those with higher frequencies are called "Diffusons", two regimes that have distinctive propagation properties: see Allen et al. [58]. In the present work such eigen-states have been referred to as extended states. The results of Figure 6 demonstrate that there exists an approximate frequency threshold above which the environment of the eigenstates has generally a compressive hydrostatic pressure, an increased bulk modulus, and strong scatter in the lowest eigen-shear. Whether or not this frequency threshold correlates with the phonon

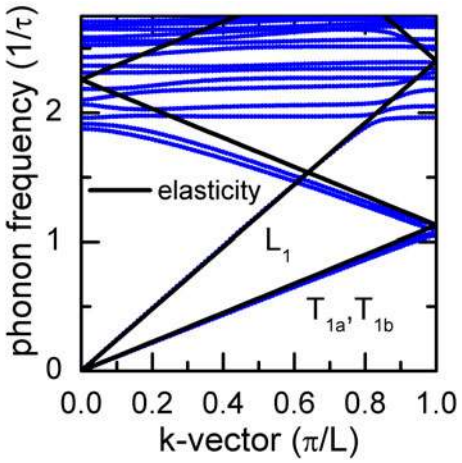

Fig. 7. (Color online) The band structure of sample 0d. Both the transverse and longitudinal acoustic modes predicted by isotropic elasticity using the sound velocities derived from equations (24) and (25) with the relaxed elastic constants of Table 2 are also shown.

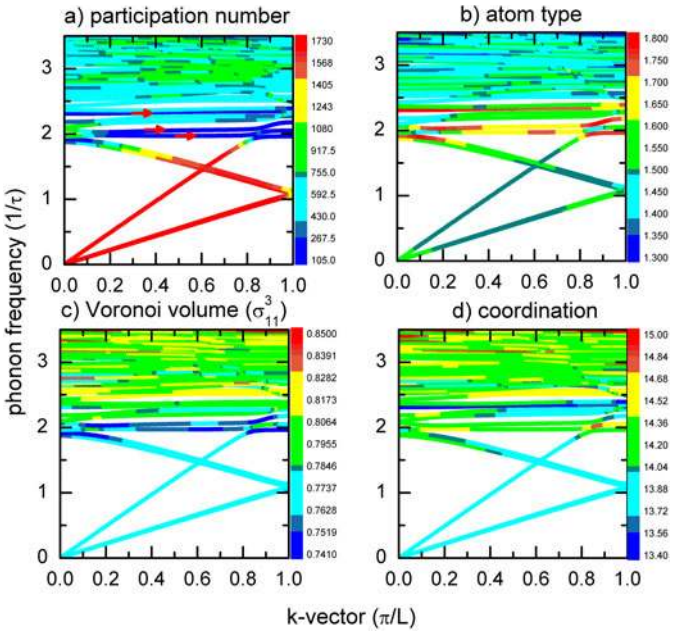

Fig. 8. (Color online) The band structure of sample 0d colour-coded according to (a) participation number, (b) atom-type, (c) local Voronoi volume, and (d) coordination.

mobility edge frequency is an interesting topic for further investigation and will not be considered in greater detail in the present work.

3.2.2 Phonon band-structure

Figure 7 displays the band structure in the first Brillouin zone along one particular simulation cell coordinate for the low frequency Boson-peak regime for sample 0d (Fig. 4b). Similar results are obtained when $\boldsymbol{k}$ is chosen to point along orthogonal (Cartesian) directions, indicating the approximate isotropy of even the smallest sample presently considered. Also plotted are the Brillouin-zone-folded transverse T_{1a}, T_{1b} and longitudinal L_1 dispersion modes predicted by isotropic elasticity using equations (24) and (25) with the relaxed elastic constants shown in Table 2. In Figure 7 there exist two distinct regimes of frequencies, a lower frequency regime exhibiting almost linear dispersion that is well described by the elastic continuum picture, and at higher frequencies a density of almost flat bands that are presently referred to as dispersionless modes. These begin at frequencies beginning at approximately $\Omega_{\rm OBP}$ ($\approx$1.9). Such modes, whilst quite flat, clearly hybridize with the accoustic branchs in the (ω, k) regions predicted by elasticity. This is most evident for the longitudinally polarized mode (at $k \approx \pi/L$ and $\omega \approx 2$), but less clear for the transverse polarization (at $k \approx 0$ and $\omega \approx 2$) region, indicating the latter accoustic mode is strongly affected by the dispersionless modes. That the accoustic branches extend well into the band of dispersionless modes is better seen in Section 3.2.4 which calculates the structure factor for these up to a wave-vector value of $4\pi/L$. It must be emphasized that the band-structure concept is an artefact of the finite (but periodic cell) used in the present simulations – in the infinite amorphous solid the Brillouin zone would contract to a single point in reciprocal space and such a figure would not be possible. Indeed for larger samples, where the Brillouin zone significantly contracts and the density of vibrational modes increase, numerical issues arise resulting in a lack of connectivity and undefined dispersion curves. It is for this reason, the $\boldsymbol{k} \neq 0$ modes are only calculated for the smallest sample, sample 0d.

In Figures 8 and 9 the dispersion curves have been colour-coded according to the PNW local quantities of the particular mode $(n, \boldsymbol{k})$, the value of which may be inferred from the neighbouring colour bar of each panel. Figure 8a displays the band-structure colour-coded according to the participation number of each mode. Inspection reveals that the number of atoms participating in the eigenstates of the linear dispersion regime (below $\Omega_{\rm OBP}$) is equal to the number of atoms in the sample. Thus, as expected, the acoustic branches involve close to all atoms in the sample. On the other hand, those dispersionless modes close to the band-edge (at $\approx\Omega_{\rm OBP}$) involve a significantly reduced number of atoms, as already seen in the low frequency part of Figure 4b. In particular, three band-edge modes are seen to involve approximately 100 atoms and are indicated by red arrows in Figure 8a.

Figure 8b displays the band-structure coloured according to the PNW atom type. Since all atoms participate in the acoustic branch, the linear dispersion regime involves atoms of both types. However at the band-edge atoms of type '2' tend to dominate, particularly for the three arrowed dispersionless modes. Figures 8c and 8d now show respectively the band-structure coloured according to the Voronoi volume and coordination. Again anomalies exist at the band-edge when compared to the bulk averages of the acoustic modes. In terms of the Voronoi volume the arrowed dispersionless modes exist in regions of slightly

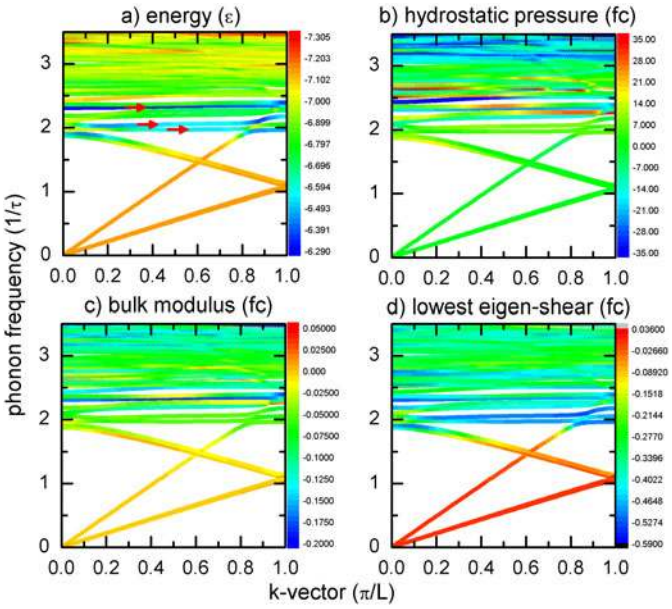

Fig. 9. (Color online) The band structure of sample 0d colour-coded according to local (a) energy, (b) hydrostatic pressure, (c) bulk modulus, and (d) the lowest local eigen-shear modulus. (b) to (d) are colour coded in terms of the fractional change (fc) with respect to the corresponding globally averaged value.

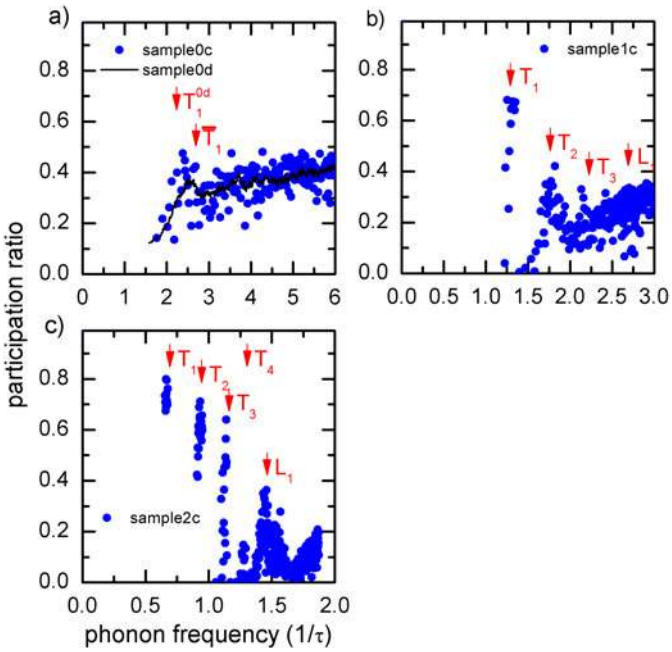

Fig. 10. (Color online) Participation ratio in the low frequency regime for the three different sized samples considered in the present work. Indicated are the predicted peaks corresponding to the [100] (T_1,L_1), [110] (T_2), [111] (T_3) and [200] (T_4) acoustic branch wave-vectors. In a) the average participation ratio derived from seven realizations of size sample 0 using quench rate η_1 is also shown.

reduced volume when compared to the average volume per atom; however from inspection of Figure 3b these values are in the upper tail of the type '2' distribution of Voronoi volumes. On the other hand, in terms of coordination, only the upper-frequency arrowed dispersionless mode has a significantly decreased coordination.

Figure 9 shows the band-structure coloured according to the PNW local energy, hydrostatic pressure, bulk modulus and lowest eigen-shear modulus. In terms of energy, Figure 9a, the arrowed band-edge modes are considerably less negative than the bulk averaged values of the acoustic branches. Figure 9b displays the band-structure coloured according to the local hydrostatic pressure, which is displayed as a fractional change with respect to the globally averaged local value. In terms of local hydrostatic pressure, the arrowed band-edge states have a PNW value that is not so different from the bulk averaged value. However, there do exist some other dispersionless states at slightly higher phonon frequencies that are quite different from the bulk value.

Figures 9c and 9d show the band-structure coloured according to the PNW bulk modulus fraction and the lowest eigen-shear fraction relative to their corresponding globally averaged values. Here it is observed that the band-edge dispersionless modes are in regions of reduced moduli. The correlation is strongest for the lowest eigen-shear modulus, where the values are significantly reduced compared to the global value – in fact, all three arrowed dispersionless modes exist in an environment with an average lowest eigen-shear, which is 50% less than that of the bulk averaged value.

3.2.3 Sample size dependence of the low frequency regime

How do the above results change when the simulation cell size and number of atoms are increased? Figure 10 displays the $\boldsymbol{k} = 0$ participation ratio for the low frequency regime for all three samples at their corresponding slowest quenches: (a) sample 0d, (b) sample 1c and (c) sample 2c. Due to computational restrictions, only the lowest 350 eigenvalues and corresponding eigenvectors are calculated for sample 2c. In Figure 10a, the average participation ratio derived from seven realizations of sample 0c are also shown to compare one quench rate across all three sample sizes, and also to demonstrate that the participation ratio is relatively insensitive to a particular atomic configuration. Inspection of all figures reveals that with increasing size there is a shift of modes towards lower phonon frequencies and a discrete bunching of modes emerges. Such a bunching arises due to the zone folding of the acoustic and longitudinal modes to the $\boldsymbol{k} = 0$ value. This becomes more pronounced for the larger system sizes since there is a corresponding decrease in the 1st Brillouin zone volume and thus a greater number of folds and therefore bunches for a given range of phonon frequencies. Precisely where this bunching occurs can be estimated by the simple formula, $\omega_n = 2\pi n v/L$, where v is the sound velocity of either the transverse or longitudinal $[n00]$ modes (Eqs. (24) or (25)), L is the simulation cell length along the direction of the chosen $\boldsymbol{k}$, and n is the nth $\boldsymbol{k} = 0$ zone fold.

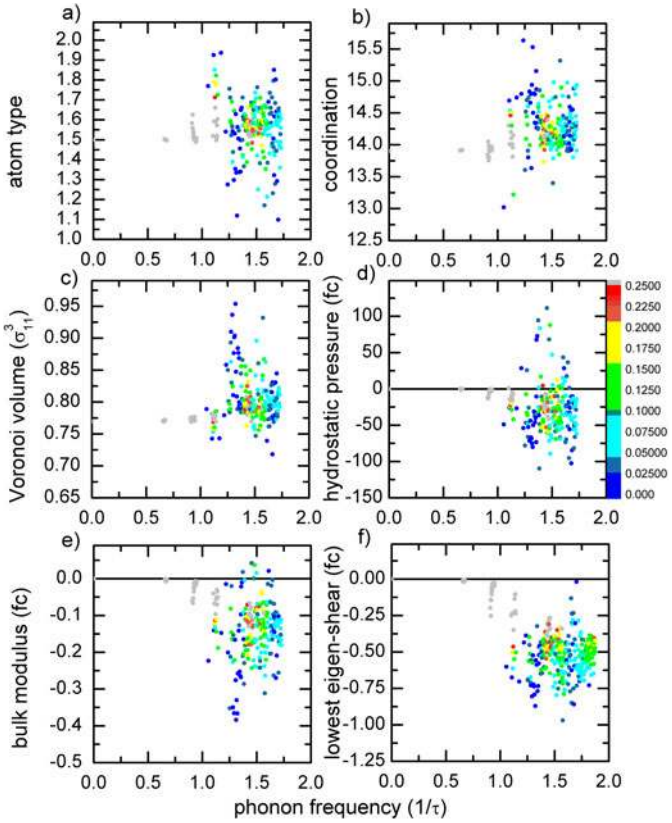

Fig. 11. (Color online) Scatter plots of participation-number-weighted (a) atom type, (b) coordination (c) local Voronoi volume, (d) local hydrostatic pressure, (e) local bulk modulus and (f) lowest eigen-shear as a function of corresponding phonon eigen-frequency for sample 2c. Data is colour coded according to the participation ratio for each corresponding mode, see colour bar.

A similar estimate can be made for the $[nn0]$ and $[nnn]$ modes for $n = 1$. The resulting predictions are marked in Figure 10 by red arrows for both the transverse and longitudinal acoustic branches. It is found that such a calculation gives a quite good estimate for the lowest non-zero frequency, with $n = 1$ for the transverse mode – this is particularly the case for the largest sample (sample 2c), Figure 10c, where the location of the [100], [110], [111] and [200] transverse modes, and the [100] longitudinal mode are well predicted. Moreover for this sample, the number of states within each bunch corresponds to the expected multiplicity of the modes, where for the $[n00]$ transverse mode it is twelve, for the $[nn0]$ transverse mode it is twenty four, and for the $[nnn]$ transverse mode it is sixteen. For sample 1c, the [100] mode had the correct multiplicity. It was however not possible to reliably count the higher wave-vector modes in sample 1c (and also all modes in sample 0d) due to strong mixing with additional dispersionless modes.

Figure 11 now shows the PNW local atomic properties for the low frequency (Boson-peak) regime of sample 2c. The data is colour-coded according to the corresponding participation ratio value; points having a participation ratio greater than 0.25 are coloured grey. Inspection of Figures 11a to d reveal no clear trend for those modes with a significantly reduced participation ratio. However, this is not the case for Figures 11e and 11f, which demonstrate a clear trend that almost all states with a participation ratio less than 0.25 exist in regions with a reduced bulk modulus and lowest eigen-shear modulus irrespective of the type of atom. This is particularly the case for those states having a very small participation ratio.

3.2.4 Transverse and longitudinal structure factors

The nature and extent of the acoustic branches for frequencies above the band-edge ($>\Omega_{\mathrm{OBP}}$) is difficult to determine due to the high density of dispersionless modes. Indeed the first Brillouin zone fold of the longitudinal mode cannot easily be identified via only the band-structure in Figures 8 and 9.

Further insight into the acoustic branches seen in Figures 8 and 9 may be gained via the calculation of the corresponding dynamical structure factors: equations (12) and (13). The upper two panels of Figure 12 display the transverse and longitudinal dynamical structure factors for sample 0d, for values of $\boldsymbol{k}$ spanning the first four Brillouin zones along the same reciprocal space direction as that used in Figures 8 and 9. In these figures only the interference terms of equations (12) and (13) are plotted; that is, the normalization factor ω^2/k^2 is omitted. Inspection of these figures, which directly reveal the dispersion properties of transverse and longitudinal sound (giving a result that is not so dependent on the (artificial) Brillouin zone boundaries), demonstrates that the transverse modes strongly broaden at the onset of the dispersionless modes, whereas the longitudinal mode is only weakly affected by their presence extending deeper into the band of dispersionless states. The two lower panels display the same data, but are now coloured using a logarithmic scale to emphasize the role of the underlying band-structure. The transverse and longitudinal linear dispersion curves predicted by elasticity are also shown as dashed lines.

The experimental (transverse) structure factor exhibits important differences to those presently simulated, where gradual broadening with increasing wave vector is observed in experiment as opposed to the abrupt occurence of broadening seen in Figure 12 at a frequency corresponding to the onset of the dispersionless modes. Indeed, experimentally for the transverse acoustic branch there are regimes of different power-law dependence for the structure factor width. Due to the finite periodic length of the used simulation cell, there exists a relatively short length-scale above which the system is homogeneous, with longer wavelengths than this seeing an effective elastic continuum and therefore perfect linear dispersion without broadening. This effective elastic medium is characterized by the relaxed elastic constants of the conventional cell calculated in Section 3.1, and the corresponding linear dispersion relation plotted in Figure 8a. Thus, as with a $\boldsymbol{k} = 0$ calculation, calculations at $\boldsymbol{k} \neq 0$ are unable to capture correctly the scattering of sound in

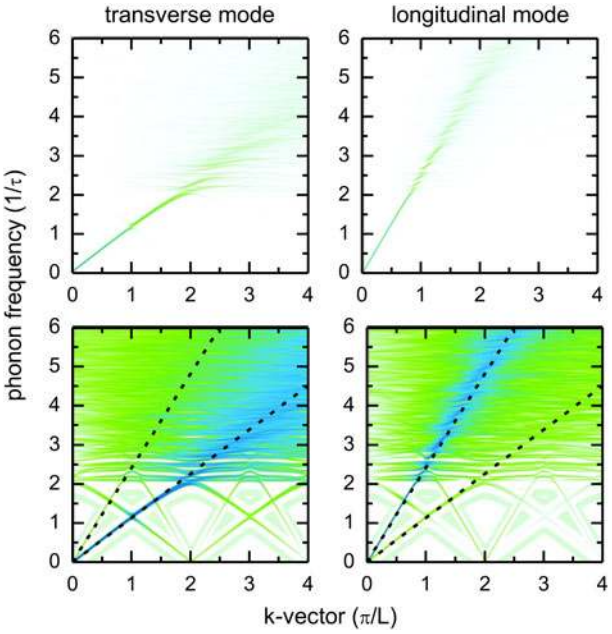

Fig. 12. (Color online) The upper two panels display the structure factors of the transverse and longitudinal acoustic modes. The two lower panels display the same data using a logarithmic shading scheme to emphasize the underlying band structure. In the lower panels, the linear dispersion relations using the sound velocities derived from equations (24) and (25) with the relaxed elastic constants of Table 2 are shown as dashed lines.

a truly bulk amorphous solid when the wavelengths are larger than that of simulation cell size. It is only when the wavelength is smaller than the simulation-cell size and the corresponding frequency is at and beyond that of the dispersionless modes, that explicit broadening occurs due to the atomic scale disorder. In this regime the broading of the transverse and longitudinal branches increases with increasing wave-vector – see the lower panels of Figure 12.

4 Discussion

The previous simulation work of Schober and Oligschleger [16] has shown that for the $\boldsymbol{k} = 0$ modes, the low frequency eigenstates are a mixture of propagating acoustic modes and localized vibrational modes. These states are referred to as quasi-local states since by virtue of their propagating component, the degree of localization is sample-size dependent and therefore not truly localized as is the case for the high-frequency modes seen in Figure 4. In reference [16] such a mixing was established by developing a numerical de-mixing procedure to extract from their eigenstates both a propagating and a localized component. Such a mixing of propagating acoustic and localized modes occurs, in part, because their corresponding characteristic frequencies are close in value, resulting in a strong interaction. It is such quasi-local eigen-states that have been observed in the low frequency regime of Figures 4 to 11 of Section 3, and it is these that are responsible for the low frequency enhancement of the vibrational density of states seen in Figure 4b referred to as the Boson peak.

Rather than performing such a de-mixing procedure, the present work has exploited the property that occurs when two states are less close in frequency, coupling between them is reduced, and the resulting eigenstates can sometimes have either a strongly propagating or strongly localized component. Such behaviour usually occurs at band-edges, where due to finite-size constraints, propagating modes are unable to exist within certain frequency intervals. This has been the primary advantage of calculating the $\boldsymbol{k} \neq 0$ modes, since away from both the Brillouin zone centre and the first Brillouin zone edge, a low frequency band-edge dispersionless state will interact less strongly with the acoustic branches. This is best seen in Figures 8 and 9, where those dispersionless modes at the band-edge (Ω_{OBP}), and away from the zone centre and Brillouin zone edge involve a significantly reduced number of atoms. For the case of the largest sample, sample 2, where for the present work no $\boldsymbol{k} \neq 0$ data has been calculated, the band-edge effect is still well evident, since many of those states with smaller participation numbers exist at the edge of the frequency bunches seen in Figures 10 and 11. Indeed this $\boldsymbol{k} = 0$ effect is also seen in the participation numbers of sample 0 and sample 1 (Fig. 10), where phonon eigenstates on the low frequency side of the predicted folded acoustic branch frequency (ω_1 in Sect. 3.2.3) involve a reduced number of atoms.

These trends may be observed by direct inspection of the spatial structure of the band-edge eigen-states. Figure 13 displays the spatial structure of several phonon eigen-states from sample 0d. In particular, they are those eigen-states with the twelve lowest phonon frequencies at $|\boldsymbol{k}| = \pi/(2L)$: the mid-way point of the band-structure shown in Figures 8 and 9. To visualize an eigenstate, each atom is coloured according to a number between zero and unity, which represents the magnitude of the local atomic polarization divided by the maximum value of the corresponding eigen-state. The local atomic polarization component, ν, of atom i and eigen-state n is given by $u^{\nu}_{j,n}$ of equation (8). Thus the atomic colouring indicates $|\boldsymbol{u}_{j,n}|/|\boldsymbol{u}_{j,n}|_{max}$ for each atom. Hence an eigen-state which is equally distributed on all atoms will result in all atoms having a colouring equal to unity, whereas an eigenstate localized entirely on one atom will have a colouring equal to unity for that atom with all other atoms having a colouring equal to zero. The actual colouring scheme is according to the colour-bar shown at the bottom left-hand corner of Figure 13j. With the aid of Figure 8a, the first two eigenstates (ordered in terms of ascending phonon frequency) at the mid-point ($|\boldsymbol{k}| = \pi/2L$) constitute the two transverse acoustic branches: Figures 13a and 13b. Inspection of these figures reveals that these eigenstates are indeed de-localized over all atoms within the sample. However, closer inspection reveals that it is not entirely homogeneous: there are a number of distinctly white atoms in the figures. The third eigenstate corresponds to the single longitudinal mode and is shown in Figure 13c. Again all atoms contribute to this eigenstate, however a certain

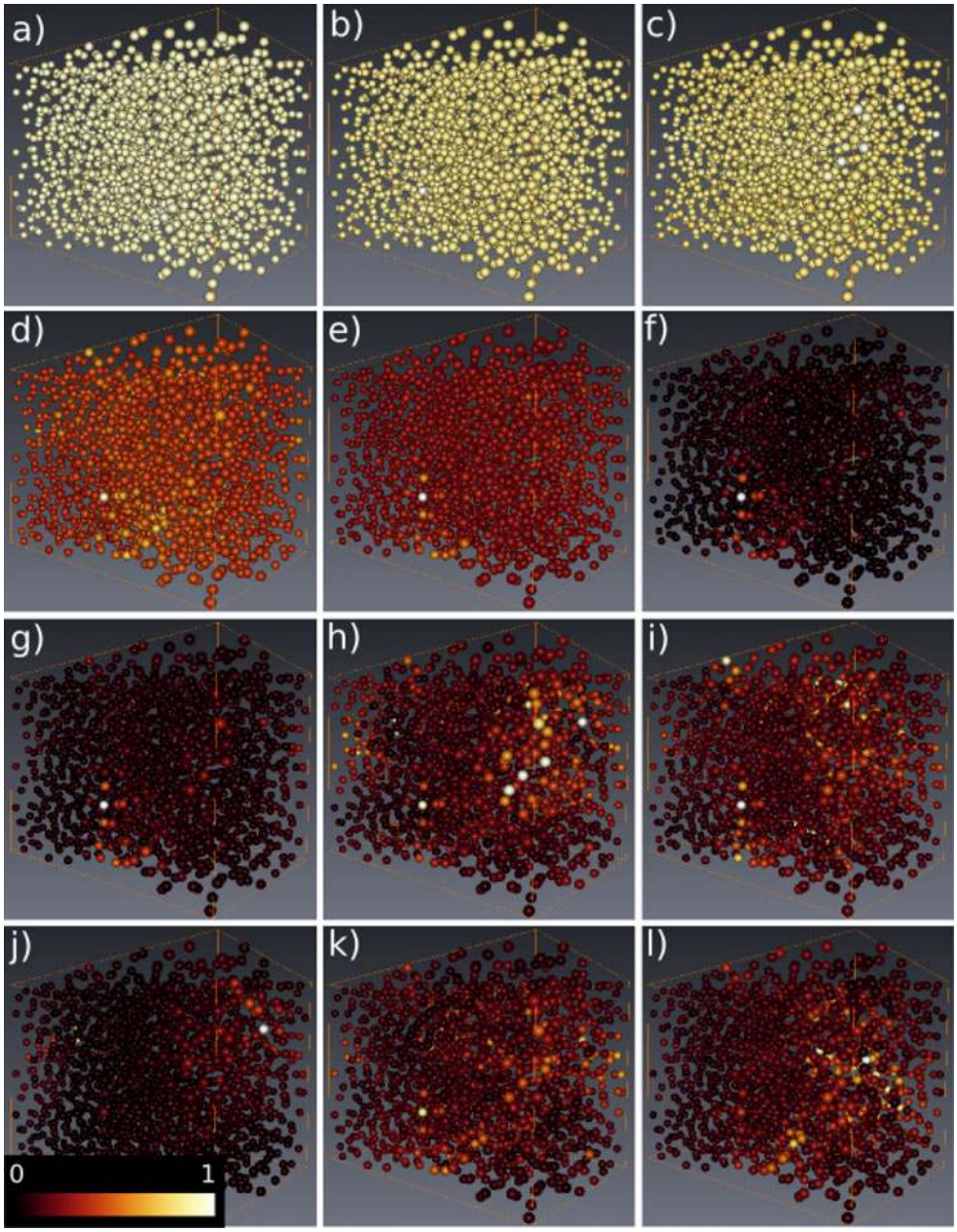

Fig. 13. (Color online) Atomic visualization of the eigenstates with the 12 lowest phonon eigen-frequencies at $|\boldsymbol{k}| = \pi/2L$ for sample 0d. Atoms are coloured according to the magnitude of the local polarization vector divided by the maximum magnitude for the corresponding eigen-state (see inset of (j)).

degree of heterogeneity is apparent. The heterogeneity seen in the accoustic branches relfects the variation in the local moduli, as evidenced by the relaxed bulk elastic moduli (Tab. 2) that describe well the linear dispersion of these modes.

The next two eigenstates, Figures 13d and 13e, correspond again to the two transverse modes which have been folded into the first Brillouin zone. Whilst these acoustic modes still involve all atoms within the sample, the degree of heterogeneity has clearly increased, where now a cluster of atoms begin to dominate. For each of the two transverse modes, the regions where such clusters of atoms occur are not so dissimilar. The next two eigen-states (Figs. 13f and 13g) are clearly confined to a few atoms. Indeed, Figure 8a reveals that these two states correspond to the band-edge states close to Ω_{OBP} and are indicated (in Fig. 8a) via the two lower-most red arrows. The next five eigen-states shown in Figures 13h to 13l display modes that are strongly heterogeneous but distributed over the entire sample. The eigen-state visualized in Figure 13j is well confined to a few atoms and is the eigen-state indicated by the upper-most red arrow in Figure 8a. Overall, Figure 13 gives examples of the mixing of propagating modes with that of non-eigenstate localized vibrational

modes, since the quasi-local modes seen in Figures 13f, 13g and 13j exist with a varying level of contribution in all the states shown.

Figure 2e demonstrates that there exist regions within the sample where the local eigen-shear is close to zero or even negative. A negative local eigen-shear formally implies that upon performing the appropriate uniform distortion on only those atomic bonds contributing to the local modulus, a reduction in the corresponding local energy of the volume element is seen. Thus, when isolated the atomic arrangement is unstable. However this does not necessarily entail that the local environment embedded within the solid is unstable since the surrounding atoms (not all of which contribute to the particular negative eigen-shear) would need to accommodate the distortion for the instability to grow. If the surrounding matrix is stable with respect to this distortion the net-effect of a local negative eigen-shear would at most involve an effective local softening for the particular distortion in that region. This could systematically be investigated by coarse-graining the volume partitioning, as was done in reference [47].

The picture that therefore emerges from the present work is that the spatial extent of the quasi-localized modes is influenced mainly by the eigen-shear modulus landscape of the material. In particular, such modes tend to exist in regions of reduced eigen-shear modulus. It is therefore expected that the non-eigenstate localized vibrational modes will be of predominantly transverse character. To what extent a particular spatial region of reduced eigen-shear will couple to a propagating mode will depend not only on the closeness of their characteristic vibrational frequencies, but also on whether the corresponding shear distortion associated with the eigen-shear mode is compatible with that of the propagating mode's polarization. It is therefore unsurprising that it is the transverse acoustic branch that is most sensitive to the presence of such modes, as seen in the structure factor calculation of Section 3.2.4, Figure 12, and in the previous work of reference [23]. Indeed at the most simple level of local approximation, via equations (24) to (25), the transverse branches only couple to the appropriate local elastic shear moduli, whereas the longitudinal branch couple to both shear and dilatational modes. Since variations in the local bulk modulus are less than that of the local elastic shear moduli, this somewhat dilutes the effect on the longitudinal acoustic branch, of a landscape of strongly varying local elastic shear moduli.

How might the sample size of an atomistic simulation be related to this scenario? With increasing system size, there will be an increased possibility that larger spatially connected regions of reduced shear moduli will occur, with correspondingly lower characteristic vibrational frequencies. Such modes are then able to couple with the appropriate lower-frequency (and therefore longer wavelength) propagating modes and the band-edge, so well defined in the present work by Ω_{OBP}, will become less sharp. Indeed, in the present work, the acoustic branches are initially perfectly linear (apart from Brillouin-zone boundary effects) and are only non-negligibly perturbed when their vibrational frequency is close to or above Ω_{OBP}. For systems much larger than considered presently, it is envisioned that the existence of multiple and extended regions of reduced shear modulus would manifest itself as a far less abrupt modification of the dispersion relations of the acoustic branches, as seen in experiment and finite molecular dynamics simulations of large two-dimensional systems [23], from which the continuous Bose-peak structure of the VDOS emerges at a characteristic frequency that is now known to correspond to the Ioffe-Regel frequency. This is the frequency at which the scattering length characterizing the interaction between the propagating mode and its environment is equal to the wavelength of the propagating mode.

For the current range of simulation cell sizes considered, the upper limit of the spatial extent of such localized (non-eigenstate) vibrational modes is set primarily by the size of the simulation cell. Figures 13f, 13g and 13j indicate that several tens of atoms would be involved in the underlying localized vibrational modes. In the larger samples, sample 1 and sample 2, such atom numbers can be somewhat larger as revealed by the participation number of Figure 10. For much larger simulation cell sizes (currently computationally intractable) the upper limit for the spatial extent of such modes might be related to the spatial extent of a connected region of low eigen-shear elastic moduli. The size of such regions is expected to be limited by issues of local mechanical instability, which leads to a thermal and/or stress-driven local transformation relaxing the structure to a locally stiffer environment. Indeed, for the samples produced at the larger quench rates, sample 0a and sample 0b, a number of eigen-frequencies well below ω_{OBP} were seen, corresponding to well-localized dispersionless eigen-states. At the slower quench rates these modes disappear producing the gap of the magnitude seen in, for example, sample 0c and sample 0d (Fig. 10a). Interestingly, these additional modes often occur at a frequency corresponding to the first intersection of the transverse branches with the Brillouin zone edge at $|\boldsymbol{k}| = \pi/L$.

The eigen-frequencies and corresponding eigen-states arise from the diagonalization of the eigen-value equation, equation (8). Thus the structure of the Hessian determines the vibrational modes of the system and the question arises, what aspect of the Hessian in the present work is responsible for the Boson-peak behaviour? By resetting all the masses to unity, the so-called mass disorder component due to the effective randomly distributed atomic masses is removed. In doing so, and subsequently diagonalizing the Hessian, it was found that there is little effect on the existing quasi-local vibrational modes, suggesting that the origin of their existence lies in the explicit disordered structure of the Hessian determined from the binary LJ interaction.

Figure 14a plots the distribution of the trace of the on-site 3×3 block diagonals of the Hessian for both atom-types in units of ε/σ^2, indicating that there are no on-site negative terms and that the distributions for both atom-types are quite similar. Figure 14b now plots the three distributions of the trace of the off-diagonal Hessian

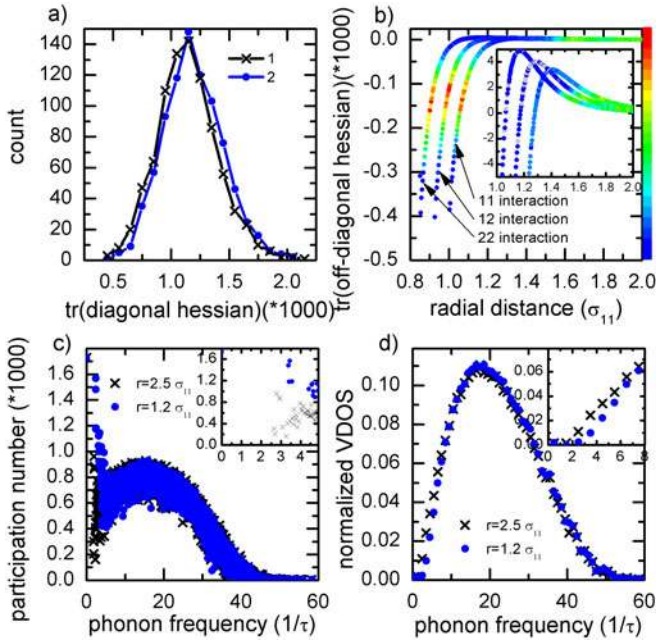

Fig. 14. (Color online) (a) Distribution of the trace of the on-site Hessian resolved for atom-type, (b) distribution of the trace of the off-diagonal Hessian as a function of radial distance in which data points are colour-coded according to frequency of occurrence, (c) participation number for a normal and short-range Hessian and (d) its corresponding VDOS normalized to three. The data is derived for sample 0d.

blocks between atoms of type '1' and '1', type '2' and '2' and types '1' and '2' as a function of radial distance between the atoms. Thus Figure 14b displays three curves as a function of radial distance, which are colour-coded according to the frequency of occurrence for that particular radius, where red represents the maximum value of the distribution and blue its minimum; for intermediate values the colour-bar to the right of Figure 14b can be consulted. Inspection of Figure 14b reveals that for each bond type, there exists a large peak in the distribution in the first neighbour shell for $r < 1.2\sigma$ and a secondary weaker and broader peak in the distribution for $r > 1.4\sigma$. Indeed, the distribution for such off-diagonal terms as a function of radial distance is nothing more than the type resolved pair-distribution function seen in Figure 3a. Moreover, the three curves seen in Figure 14b are simply the polarization traces of equation (5). The negative values of the trace of the off-diagonal blocks seen for $r < 1.2\sigma$ correspond to effective positive spring constants, whereas the trace of the off-diagonal blocks seen for $r > 1.4\sigma$ would correspond to longer-range effective spring constants, which have a negative sign.

How do these longer-range off-diagonal components of the Hessian affect the low frequency vibrational properties of the system? This may be investigated by excluding these long range off-diagonal components beyond (say) $r > 1.2\sigma$, and diagonalising the resulting modified Hessian. It is noted that the original atomistic structure (as obtained when using a $r_c = 2.5\sigma$) is held fixed, that is there is no relaxation performed using the corresponding truncated interaction potential. Figure 14c displays the resulting participation number for sample 0d. In this figure, the participation number distribution for the original Hessian is also shown for comparison. The inset shows a blow-up of the low frequency regime. It is observed that for the truncated Hessian the low frequency modes containing a reduced number of atoms are entirely absent. By binning the resulting distribution of phonon frequencies, the corresponding truncated VDOS is obtained and compared to the original shown in Figure 4a, and it is seen that there is a reduction in the number of low frequency states when compared to the original. Importantly, the truncation of the Hessian does not markedly effect the intermediate to higher phonon-frequency regime, nor the linear dispersion of the low frequency acoustic branches. The latter is due the global elastic stiffness moduli not significantly changing apart from an overall stiffening; see Table 3, which lists the global elastic moduli calculated using equation (15) for both inter-atomic potential cut-offs.

Table 3. Table listing the global elastic stiffness moduli (in units of $\varepsilon/\sigma_{11}^3$) for sample 0d for two Lennard-Jones cut-off radii. Shown are the Bulk modulus and isotropic shear modulus and also the five Kelvin eigenshears. For a perfectly isotropic medium, all five Kelvin eigen-shears would equal 2μ.

Modulus	$r_c = 2.5\sigma_{11}$	$r_c = 1.2\sigma_{11}$
K	78.96	88.24
μ	48.18	50.46
μ_1	91.89	96.58
μ_2	92.16	96.89
μ_3	95.13	99.72
μ_4	96.24	100.83
μ_4	98.34	102.8

The above observations indicate that for the present work the origin of the quasi-local vibrational modes, and therefore the Boson-peak structure of the VDOS, does not lie in the mass disorder, the diagonal disorder, nor the short-range off-diagonal disorder of the Hessian. Rather, its origin lies in the long-range off-diagonal Hessian disorder which, by virtue of a decreasing negative LJ interaction with increasing distance, results in a distribution of long-range negative effective spring constants. Although the magnitude of these negative spring constants is small when compared to the short-range positive spring constants, their presence has clearly a non-negligible effect. This is most likely due to the large number of inter-atomic distances available at this regime of radii. Moreover, even though such long-range components contribute to only a minor softening of the bulk elastic moduli (Tab. 3), detailed inspection of the change in the eigen-shear moduli distribution (not shown) reveals that the tail of negative eigen-shear moduli seen for atoms of type '2' is almost entirely absent upon their removal, due to the general shift of all the moduli (of both atom-types) to higher stiffness values.

Thus, when using a potential of the form of equation (1), the structural origin of the quasi-local vibrational modes lies in the disorder associated with a length scale

beyond that of the coordination shell environment. This conclusion is expected to be applicable to more general models of pairwise/dispersive cohesion, since to stabilize a material system, any effective pair-wise potential with a short-range repulsive character must have a long-range form that is attractive, the latter of which will naturally lead to negative long-range effective spring constants. Although this property might be a sufficient condition, it is clearly not a necessary condition since purely repulsive potentials in which the atomic system is stabilized via an external compressive stress also admit such low frequency modes [13,14]. In such soft pair-wise systems it is expected that the soft nearest-neighbour spring constants will be responsible for the anomolous low frequency modes, leading also to spatial regions within the glass that have spring constants and eigen-shear moduli that are negative.

Finally, as in experiments [59,60], the present work finds that higher cooling rates yield an increase in atomic volume, as well as a decrease in shear modulus, which can be understood as an increase in structural defect concentration due to reduced structural relaxation in metallic glasses when being quenched quickly. It has further been reported in the experimental literature that the Poisson ratio, which provides a fundamental connection to the malleability of glasses [61], increases for larger cooling rates [60–62]; a trend that is not clearly distinguishable in the present simulation work when equation (15) is used to calculate the global elastic moduli, nor for the relaxed moduli listed in Table 2. Given that a locally reduced atomic density is widely believed to control the deformation of metallic glasses [63], it is interesting to note that the quasi-localized low frequency modes correlate with such a local atomic environment of larger volume. Since a structural state of increased free volume (globally a higher concentration of structural defects) more readily can accommodate local shear, such sites are generally believed to have a low energy barrier for a cooperative inelastic transition, of which the size again is a function of Poisson ratio [64].

Even though no plastic straining was performed within the present work, the fact that the quasi-localized low frequency modes manifest themselves at sites of strongly reduced local elastic shear moduli and increased free volume, poses the interesting question to what extent those sites identify local atomic regions prone to firstly generate plastic transformations? This would mean that the vibrational eigen-modes causing the Boson-peak anomaly could potentially be correlated with atomic sites that are responsible for mediation of strain in a disordered glassy structure, a fundamental question that forms the basis for the continuation of this work.

Work suggesting such a link has been done by a variety of groups. The work of [21] found that for athermal/high stress deformation simulations irreverible atomic rearrangements were quite localized and therefore did not correlate in an obvious manner with those extended regions in which strong non-affine elastic displacements occured. It was suggested that a more likely pre-cursor signature of plasticity would be the more localized regions of negative shear moduli found by Yoshimoto et al. [65]. Indeed, Mayr [47] has found that as the temperature approaches the glass transition temperature of stress-free model glass samples, thermally activated, more extended irreversible structural transtitions do occur that are spatially correlated with regions of negative local eigen-shear modulus. That such "shear transformation zones" are more extended at low stresses was also confirmed by the application of potential energy landscape exploration alogirthms to mode glass systems [66,67]. That a thermal component might play a fundamental role has also been suggested in atomistic simulation work in model super-cooled liquids [68], in which spatially fluctuating local Debye-Waller factors might be an indicator of whether or not a region is likely to undergoe significant displacement. Indeed, in the condensed-phase regime of an amorphous solid, such thermal quantities, are intimately linked to the vibrational properties studied here.

5 Concluding remarks

In conclusion, the present work reports on an investigation of the vibrational properties of model binary structural glasses prepared by a molecular dynamics quenching procedure. By diagonalizing the resulting Hessian of the zero Kelvin structures to obtain the normal modes of the system, the harmonic vibrational properties could be investigated in detail and related to the atomic structure of the computer generated samples. While the high-frequency localized modes were investigated also, the emphasis of this work lies in a study of the low frequency properties, which manifest themselves as the experimentally accessible Boson-peak anomaly in the vibrational density of states. The quasi-localized eigen-modes that underlie this enhancement of the low frequency vibrational density of states were investigated in detail via their participation-number-weighted local atomic property values and it was found that such normal modes are strongly biased to regions of the atomic structure that are characterized by considerably reduced local elastic shear moduli. A lesser correlation was found in terms of regions of increased local free volume, local tensile hydrostatic pressures, and reduced local elastic bulk moduli. By inspection of the Hessian structure, it was found that it is the long-range off-diagonal disorder structure that is responsible for the quasi-localized modes. Such long-range off-diagonal structure is characterized by a distribution of negative effective spring constants whose existence is the direct result of the long-range attractive nature of the LJ inter-atomic potential employed in the present simulations. Since in general a pair-wise interaction is required to be attractive in the long-range, such a finding might be quite general and play a defining role in the claimed universality of the Boson-peak form. Such a result certainly motivates further work in the field of simplified random-matrix models of lattice disorder, where now distributions of off-diagonal disorder compatible with the constraints of a pair-wise interaction may be investigated.

P.M.D. wishes to thank D. Crespo, E. Pineda, P. Bruna, J. Seranno for helpful discussions.

References

1. A. Monaco, A.I. Chumakov, G. Monaco, W.A. Crichton, A. Meyer, L. Comez, D. Fioretto, J. Korecki, R. Ruffer, Phys. Rev. Lett. **97**, 135501 (2006)
2. A. Monaco, V.M. Giordano, Proc. Natl. Acad. Sci. **106**, 3659 (2009)
3. T. Scopigno, E. Pontecorvo, R. Di Leonardo, M. Krisch, G. Monaco, G. Ruocco, B. Ruzicka, F. Sette, J. Phys.: Condens. Matter **15**, S1269 (2003)
4. T. Scopigno, J.-B. Suck, R. Angelini, F. Albergamo, G. Ruocco, Phys. Rev. Lett. **96**, 135501 (2006)
5. B. Ruffle, G. Guimbretiere, E. Courtens, R. Vacher, G. Monaco, Phys. Rev. Lett. **96**, 045502 (2006)
6. G. Ruocco, A. Matic, T. Scopigno, S.N. Yannopoulos, Phys. Rev. Lett. **98**, 079601 (2007)
7. B. Ruffle, G. Guimbretiere, E. Courtens, R. Vacher, G. Monaco, Phys. Rev. Lett. **98**, 079602 (2007)
8. B. Ruffle, D.A. Parshin, E. Courtens, R. Vacher, Phys. Rev. Lett. **100**, 015501 (2008)
9. R. Shuker, R.W. Gammon, Phys. Rev. Lett. **25**, 222 (1970)
10. G. Winterling, Phys. Rev. B **12**, 2432 (1975)
11. R.J. Nemanich, Phys. Rev. B **16**, 1655 (1977)
12. R. Biswas, A.M. Bouchard, W.A. Kamitakahara, G.S. Grest, C.M. Soukoulis, Phys. Rev. Lett. **60**, 2280 (1988)
13. B.B. Laird, H.R. Schober, Phys. Rev. Lett. **66**, 636 (1991)
14. H.R. Schober, B.B. Laird, Phys. Rev. B **44**, 6746 (1991)
15. V. Mazzacurati, G. Ruocco, M. Sampoli, Europhys. Lett. **34**, 681 (1996)
16. H.R. Schober, C. Oligschleger, Phys. Rev. B **53**, 11469 (1996)
17. H.R. Schober, J. Phys.: Condens. Matter **16**, S2659 (2004)
18. O. Pilla, S. Caponi, A. Fontana, J.R. Gonalves, M. Montagna, F. Rossi, G. Viliani, L. Angelani, G. Ruocco, G. Monaco, F. Sette, J. Phys.: Condens. Matter **16**, 8519 (2004)
19. J. Horbach, W. Kob, K. Binder, Eur. Phys. J. B **19**, 531 (2001)
20. J.P. Wittmer, A. Tanguy, J.-L. Barrat, L. Lewis, Europhys. Lett. **57**, 423 (2002)
21. F. Léonforte, R. Boissière, A. Tanguy, J.P. Wittmer, J.-L. Barrat, Phys. Rev. B **72**, 224206 (2005)
22. F. Léonforte, A. Tanguy, J.P. Wittmer, J.-L. Barrat, Phys. Rev. Lett. **97**, 055501 (2006)
23. H. Shintani, H. Tanaka, Nature Mater. **7**, 870 (2008)
24. G. Monaco, S. Mossa, Proc. Natl. Acad. Sci. **106**, 16907 (2009)
25. W. Schirmacher, Europhys. Lett. **73**, 892 (2006)
26. W. Schirmacher, G. Ruocco, T. Scopigno, Phys. Rev. Lett. **98**, 025501 (2007)
27. S.N. Taraskin, Y.L. Loh, G. Natarajan, S.R. Elliott, Phys. Rev. Lett. **86**, 1255 (2001)
28. W. Schirmacher, G. Diezemann, C. Ganter, Phys. Rev. Lett. **81**, 136 (1998)
29. V. Ilyin, I. Procaccia, I. Regev, Y. Shokef, Phys. Rev. B **80**, 174201 (2009)
30. F.J. Dyson, Phys. Rev. **6**, 1331 (1953)
31. V.L. Gurevich, D.A. Parshin, H.R. Schober, Phys. Rev. B **67**, 094203 (2003)
32. V.L. Gurevich, D.A. Parshin, H.R. Schober, Phys. Rev. B **71**, 014209 (2005)
33. D.A. Parshin, H.R. Schober, V.L. Gurevich, Phys. Rev. B **76**, 064206 (2007)
34. G. Wahnström, Phys. Rev. A **44**, 3752 (1991)
35. M. Tsamados, A. Tanguy, C. Goldenberg, J.-L. Barrat, Phys. Rev. B **80**, 026112 (2009)
36. S.K. Sarkar, G.S. Matharoo, A. Pandey, Phys. Rev. Lett. **92**, 215503 (2004)
37. G.S. Matharoo, S.K. Sarkar, A. Pandey, Phys. Rev. B **72**, 075401 (2005)
38. H.M. Flores-Ruiz, G.G. Naumis, J.C. Phillips, Phys. Rev. B **82**, 214201 (2010)
39. W. Thomson, Philos. Trans. R. Soc. Lond. **146**, 481 (1856)
40. M. Parrinello, A. Rahman, J. Appl. Phys. **52**, 7182 (1981)
41. D.J. Evans, B.L. Holian, J. Chem. Phys. **83**, 4069 (1985)
42. R.B. Lehoucq, D.C. Sorensen, C. Yang, *ARPACK Users Guide: Solution of Large-Scale Eigenvalue Problems with Implicitly Restarted Arnoldi Methods* (SIAM, Philadelphia, 1998)
43. R.J. Bell, P. Dean, Discuss. Faraday Soc. **50**, 55 (1970)
44. J.F. Lutsko, J. Appl. Phys. **64**, 1152 (1988)
45. J. Cormier, J.M. Rickman, T.J. Delph, J. Appl. Phys. **89**, 99 (2001)
46. C.H. Rycroft, G.S. Grest, J.W. Landry, M.Z. Bazant, Phys. Rev. E **74**, 021306 (2006)
47. S.G. Mayr, Phys. Rev. B **79**, 060201(R) (2009)
48. P.G. Debenedetti, F.H. Stillinger, Nature **419**, 259 (2001)
49. Y. Shi, M.L. Falk, Phys. Rev. **73**, 214201 (2006)
50. P.M. Derlet, R. Meyer, L.J. Lewis, U. Stuhr, H. Van Swygenhoven, Phys. Rev. Lett. **87**, 205501 (2001)
51. P.M. Derlet, H. Van Swygenhoven, Phys. Rev. Lett. **92**, 035505 (2004)
52. P.M. Derlet, S Van Petegem, H. Van Swygenhoven, Philos. Mag. **89**, 3511 (2009)
53. M.L. Metha, *Random Matrices*, 2nd edn. (Academic Press, San Diego, 1991)
54. A.P. Sutton, Philos. Mag. A **60**, 147 (1989)
55. P.W. Anderson, Phys. Rev. B **109**, 192 (1958)
56. W. Garber, F.M. Tangerman, P.B. Allen, J.L. Feldman, Philos. Mag. Lett. **81**, 433 (2001)
57. B.J. Huang, T.-M. Wu, Phys. Rev. B **79**, 041105 (2009)
58. P.B. Allen, K.L. Feldman, J. Fabian, F. Wooten, Philos. Mag. B **79**, 1715 (1999)
59. S.V. Khonik, A.V. Granato, D.M. Joncich, A. Pompe, V.A. Khonik, Phys. Rev. Lett. **100**, 065501 (2008)
60. A. Castellero, D.I. Uhlenhaut, B. Moser, J.F. Löffler, Philos. Mag. Lett. **87**, 383 (2007)
61. J.J. Lewandowski, W.H. Wang, A.L. Greer, Philos. Mag. Lett. **85**, 77 (2005)
62. X.J. Gu, S.J. Poon, G.J. Shiflet, J.J. Lewandowski, Scr. Mater. **60**, 1027 (2009)
63. A.S. Argon, Acta Metall. **27**, 47 (1979)
64. D. Pan, A. Inoue, T. Sakurai, M.W. Chen, Proc. Natl. Ac. Sci. **105**, 14769 (2008)
65. K. Yoshimoto, T.S. Jain, K. Van Workum, P.F. Nealey, J.J. de Pablo, Phys. Rev. Lett. **93** 1755012 (2004)
66. D. Rodney, C.A. Schuh, Phys. Rev. Lett. **102**, 235503 (2009)
67. D. Rodney, C.A. Schuh, Phys. Rev. B **80**, 184203 (2009)
68. A. Widmer-Cooper, P. Harrowell, Phys. Rev. Lett. **96** 185701 (2006)